Laboratory for Aero & Hydrodynamics
Master Thesis

Self-Sustaining Mechanisms in Wall Bounded Turbulence:
Merging & Auto-generation of Vortices

Author:
Manu Goudar Vishwanathappa,
4122801

Supervisors:
Dr.ir. G.E. Elsinga,
Dr.ir. W.P. Breugem

July 4 2012, MEAH - 265

Exam Committee:
Prof.dr.ir. J.Westerweel, TU Delft
Prof.dr.ir. Wim S.J. Uijttewaal, TU Delft
Dr.ir. G.E. Elsinga, TU Delft
Dr.ir. W.P. Breugem, TU Delft

Dedicated to my parents and sister.

ABSTRACT

The hairpin eddy model is used to explain the self-sustaining mechanisms in the outer layer of wall bounded turbulent flows. In this model, hairpin vortices auto-generate producing additional (hairpin) vortices, which form so called vortex packets. These packets are observed to populate the outer layer. Zhou et al. (1999) reported that only hairpins above a certain threshold strength can auto-generate. In this report, we explore how such a hairpin of threshold strength may come into existence. This is done by studying the interactions between two non auto-generating eddies in different scenarios. These scenarios are created based on different initial strengths, initial sizes and initial stream-wise spacing between the aligned eddies. The velocity field of the initial eddies is extracted from a direct numerical simulation database of fully turbulent channel flow at $Re_\tau = 360$ by means of linear stochastic estimation.

The two non auto-generating eddies were found to merge into a single stronger eddy when a larger upstream and a smaller downstream eddy are placed within a certain initial stream-wise distance. Subsequently, the resulting stronger eddy was observed to auto-generate new eddies. In some cases, new structures were generated even though there was no merging and stream-wise spacing was large. So there has to be another kind of interaction which results in auto-generation, as vortex-vortex interaction weakens with increasing spacing. This interaction may be between low speed streak and vortex, as both the eddies share the same low speed streak. The vortex-streak interaction happens when fluid ejected by downstream eddy is absorbed by upstream eddy. This can also occur when the stream-wise separation between two eddies is small.

Merging of eddies, thus is the viable explanation for the creation of threshold strength eddies. Moreover, it extends the auto-generation process towards a possible self-sustaining mechanism: two initial hairpins merge producing a strong hairpin, which further creates a new hairpin structure by auto-generation resulting again in two hairpins. From vortex-streak interaction, it may be concluded that low-speed streak does play a role in the generation of new structures. Hence the criterion and the mechanisms to determine the auto-generation become more complex, when two hairpins are aligned behind each other than the one mentioned (threshold strength) for a single eddy case in Zhou et al. (1999).

ACKNOWLEDGMENTS

This thesis report would not have been possible without support of many people. First and foremost I would like to express my deep gratitude to dr.ir. G.E. Elsinga, my first research supervisor, for his patient guidance, enthusiastic encouragement and useful critiques of this thesis work. I offer my sincerest gratitude to my second supervisor, dr. ir. W.P. Breugem for his constant support, guidance and invaluable assistance. My supervisors willingness to give their time so generously has been very much appreciated. I also gratefully thank them for allowing me the room to work in my own way. One simply could not wish for a better or friendlier supervisors.

I would like offer my special thanks to my good old friend, Arjun Shankar for his valuable inputs on parallel programming and on how to write an optimized code. I would also like to thank Dr. Eng. Luis Portela for many insightful discussions on vortex structure. While doing a numerical study it seem impossible not to come across computer related problems. I greatly appreciate and thank dr.ir. M.J.B.M. Pourquie for his help and initiative to keep my computer running whenever it breakdown apart from his main work.

Deepest gratitude are also due to the members of the supervisory committee, prof.dr.ir J.Westerweel and prof.dr.ir W.S.J.Uijttewaal without whose knowledge and assistance this study would not be successful.

In my daily work and life, I have been blessed with a friendly and cheerful group of friends, fellow students and PhDs. I like to thank Paul V Lunen who was a good companion from last two years. He has always been supportive and encouraging at work. I would also thank Sridevi Koonath and Arjun Shankar for being with me in all ups and downs of life here in Netherlands. I also thank all the friends and people in Aero & Hydrodynamics lab for their support directly or indirectly in finishing my thesis and many good laughs.

I am also indebted to the many countless contributors to the "Free Software/Open Source" programming community for providing the numerous tools and systems I have used to produce both my results and this thesis. I also thank André Miede for this beautiful LaTeXtemplate.

Finally, I wish to thank my parents for their support and encouragement throughout my study.

CONTENTS

LIST OF FIGURES

LIST OF TABLES

NOMENCLATURE

$(\tilde{\ })$	initial condition of ( ).
$(\ )'$	perturbation values of ( ).
$(\ )^+$	non-dimensional values of ( ) using wall units.
$-\langle u'v' \rangle$	Reynolds shear stress.
H	full channel height.
L_{ij}	linear estimate coefficients.
Re_τ	friction Reynolds number.
α	relative strength of a conditional eddy.
λ_{ci}	local swirling strength.
$\langle(\ )\rangle$	average values of ( ).
ν	kinematic viscosity.
ρ	density of fluid.
τ_w	wall shear stress.
f_{uv}	joint probability density function of occurance of u' and v'.
u_τ	friction velocity.
x	stream-wise direction.
y	wall-normal direction.
y_e^+	event vector location.
z	span-wise direction.
DNS	direct numerical simulation.
h	half channel height.
LSE	linear stochastic estimate.
Q2	quadrant 2 in u′-v′ plane.
Q4	quadrant 4 in u′-v′ plane.
TBL	turbulent boundary layer.

1

INTRODUCTION

In most of the engineering applications, we come across turbulent flows over solid surfaces like flow over car or wings of an aircraft. Due to the no slip condition at the surface, shear stress is produced which retards the fluid motion adjacent to the surface. The region associated with this is called a boundary layer (BL). The drag from the wall is responsible for a loss in energy/momentum. If the BL becomes turbulent then there is increased mixing of fluid which causes an increase in drag and hence additional loss of momentum. Hence reduction of the turbulent contribution to the drag will help in making energy efficient designs and save large amount of resources. In order to do this, it is important to understand the internal structure and dynamics of turbulent flows over surfaces. From the literature, it is observed that there are events which occur continuously and repeat in time in turbulent boundary layers. To generate these events there are mechanisms which occur repeatedly and are called self-sustaining mechanisms.

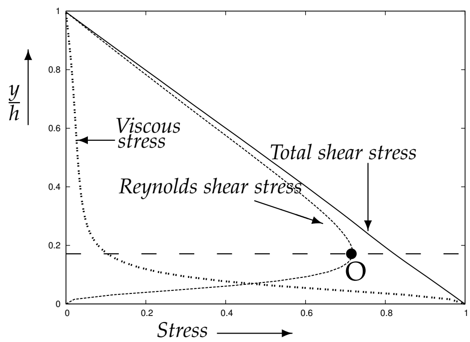

Figure 1.1: Shear stress profile normalized by half-channel height (h) and wall shear stress (τ_w).

1.1 SELF-SUSTAINING MECHANISM

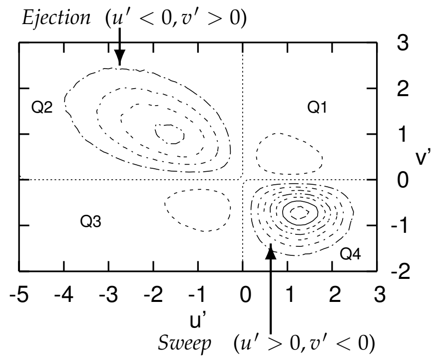

Figure 1.2: Contours of weighted Reynolds shear stress in turbulent plane channel flow given by $-u'v'f_{uv}$ at $y^+ = 103$ where f_{uv} is Joint probability density function of occurrence of u' and v'.

One of the main features of wall bounded turbulent flows is *continuous extraction and transfer of momentum from the high-velocity core/outer region to low-velocity near-wall/inner region and further dissipation into internal energy by action of viscous forces*. This mechanism of energizing the near wall region is continuous and a self sustaining process. Statistically this process is quantified with the help of turbulent fluctuations (u_i') or Reynolds shear stresses $(\rho\langle u_i' u_j' \rangle)$. In channel flows, the Reynolds shear stress $(-\langle u'v' \rangle)$[1] contribution to the total shear stress can be seen in figure 1.1. The force per unit volume on the mean flow due to $-\langle u'v' \rangle$ is given by $d(-\rho\langle u'v' \rangle)/dy$. This force is positive below point O (figure 1.1) which means the fluid is accelerated in this region. Above that point the force becomes negative leading to deceleration of fluid flow. In other words, this means

1 u', v' and w' are perturbation velocity components in stream-wise (x), wall normal (y) and span-wise (z) directions respectively

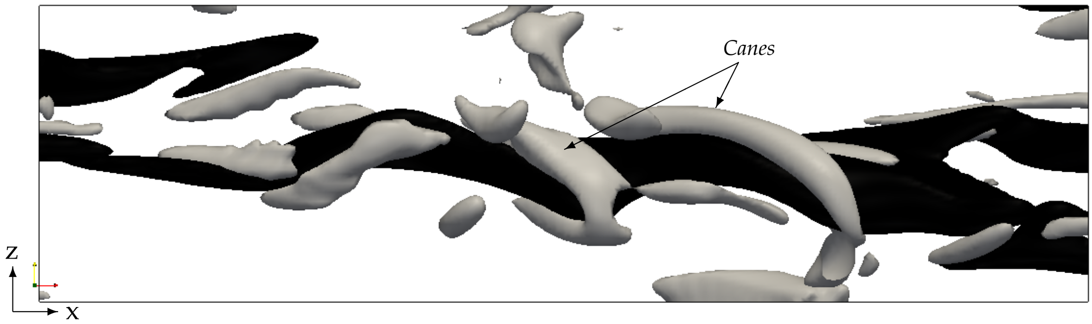

(a) Small section of turbulent channel flow. Black region corresponds to low speed streaks (regions with $u' < 0$) and canes/vortices are given by gray contours in instantaneous field of DNS.

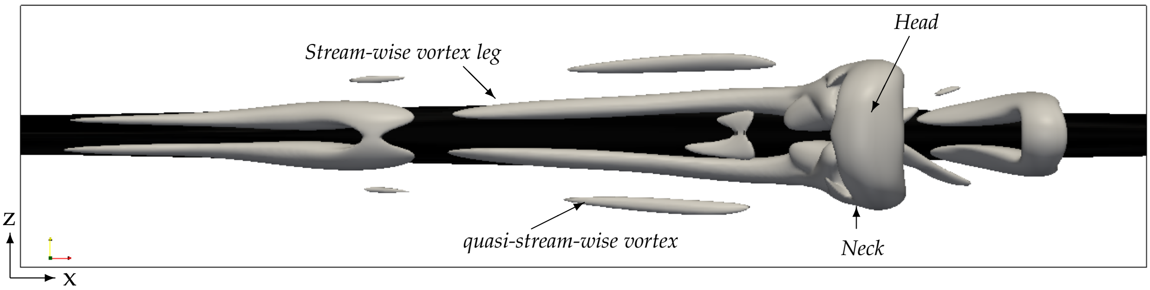

(b) Ideal hairpin vortices (gray contours) obtained from Linear stochastic estimate along with low speed streaks $u' < 0$ (black contours) and quasi-stream-wise vortex.

Figure 1.3: 2-d projection of different 3-d structures onto xz-plane in wall bounded turbulent flows. The vortices are visualized using swirling strength criterion(refer section 3.3). Above figures are not on same scale.

transfer of momentum from outer region to inner region. Figure 1.2 shows the contribution to $-\langle u'v' \rangle$ by different combination of u' and v'. The product $-u'v'$ is positive in second(Q2) and fourth(Q4) quadrants leading to positive Reynolds shear stress shown in figure 1.1. Second quadrant events ($u' < 0, v' > 0$) or Q2 events are referred as *ejections* as they correspond to lift up of low-speed fluid away from wall. Fourth quadrant events ($u' > 0, v' < 0$) or Q4 events are called *sweeps* as they move high-speed fluid towards the wall. It is important to understand the mechanisms that are responsible for creating these Reynolds shear stresses and anti-correlated velocity fluctuations.

In the process of understanding these mechanisms, investigations (see Robinson, 1991; Adrian, 2007) revealed that these ejection/Q2 events are closely associated with coherent structures like hairpins and stream-wise vortices as shown in figure 1.3 and 1.4. Figure 1.4 (from Robinson, 1991) shows the distribution of structures in different regions of wall bounded turbulent boundary layer. From here the wall bounded turbulent boundary layer will be referred as the turbulent boundary layer (TBL) for easiness. Wake region is the outer part of outer region and is mainly populated by hairpin vortices. Quasi-stream-wise vortices dominate the buffer layer where turbulent energy production rate reaches maximum and both viscous stresses and Reynolds shear stresses are important. Logarithmic or overlap re-

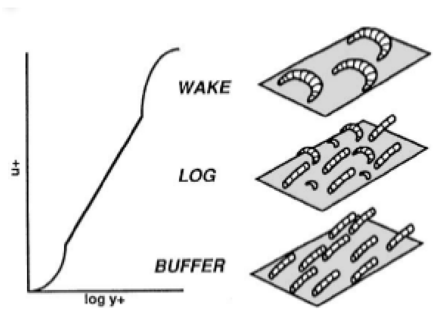

Figure 1.4: Different coherent structures present in different regions of TBL. (taken from Robinson, 1991).

gion where Reynolds shear stress is approximately constant, contains both stream-wise (lifted) and hairpin vortices. These structures are largely considered similar in turbulent pipe and channel flows and zero pressure gradient turbulent boundary layer flow (see Adrian, 2007). Hence terms TBL and channel flow are interchangeable in this report unless mentioned.

Perry and Marusic (1995) came up with a wall-wake model using eddy structures to explain the turbulent structure of boundary layer flows. Along the same lines, the above mentioned coherent structures can be used to create a model to explain the turbulent boundary layer flows. And one of the existing models to explain the presence of self-sustaining mechanisms in outer layer is the hairpin eddy model (see Adrian, 2007). This will be discussed in detail in the next section.

1.2 HAIRPIN EDDY MODEL

The hairpin/horseshoe vortex in the TBL was first proposed by Theodorsen in 1952. In this model there was an Ω shaped vortex head which was connected to legs extending in span-wise directions as shown in figure 1.5. The Secondary and tertiary horseshoes are curled up on the primary hairpin. From the figure 1.5, it can be observed that fluid flows around the vortex head which leads to ejection of fluid upstream in front of the head creating Reynolds shear stresses. But this hairpin structure was not completely accurate, further investigation of direct numerical simulation (DNS) data by Robinson (1991) indicated that hairpins are made of an Ω shaped vortex head, neck and two counter-rotating stream-wise legs as shown in figure 1.3b. But in most cases hairpins do not possess span-wise symmetry and appear to be asymmetric as shown in figure 1.3a in which case they are called *one sided hairpins* or *canes*. In this one/two sided hairpin structure, Reynolds shear stress is not only generated by the head but also by the stream-wise vortex legs. In figure 1.3b, fluid between the hairpin legs is pumped away from the wall by stream-wise vortex legs.

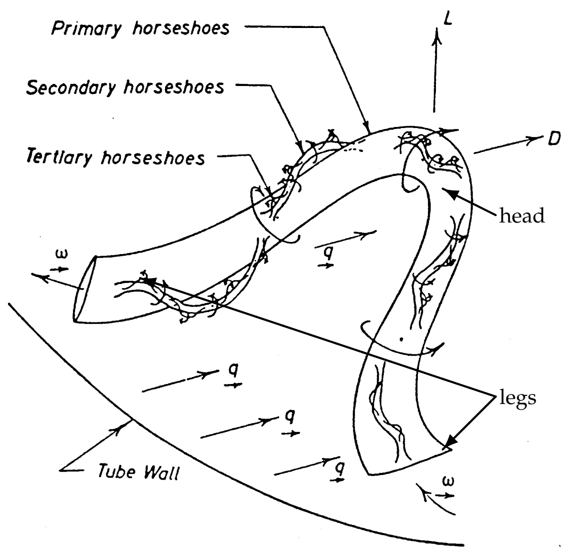

Figure 1.5: Horseshoe concept of Theodorsen (taken from Theodorsen, 1952). 'q' stands for velocity, 'L' & 'D' for Lift and Drag forces.

Experimental studies by Bandyopadhyay (1980); Head and Bandyopadhyay (1981) renewed the interest in hairpin vortices as building blocks of TBL. From experiments, they suggested that:

- The TBL was filled with hairpin vortices over a range of Reynolds numbers.
- The span-wise distance between the legs of hairpin was around 100 viscous wall units even at higher Reynolds numbers.
- As the hairpin legs grow in length and height, the head extends to the outer layer from buffer layer keeping same span-wise distance between legs.

If this mentioned growth of the hairpins is considered then at very high Reynolds numbers the height (wall normal) to width (span-wise) ratio becomes very high. Such thin eddies cannot possibly survive among other strong turbulent structures. And also in the outer region they have to interact with the other eddies as their size grows. So the explanation of how these hairpins come into existence, grow and organize themselves in the TBL in this model was not completely clear.

Head and Bandyopadhyay (1981); Smith (1984) reported that these hairpins are organized and occur in groups in the stream-wise direction (i.e, the direction of flow). High resolution velocity field data by particle image velocimetry of the TBL by Adrian, Meinhart, and Tomkins (2000) shows a strong experimental evidence for the organization of hairpins. Their main observations were:

- Hairpin vortices are aligned behind each other in series in the stream-wise direction as shown in figure 1.6.
- Below the head of the hairpins, fluid from downstream is pushed towards upstream hairpin. This leads to a long region of low speed fluid or low speed streak ($u' < 0$) below the hairpin head as shown in figure 1.6. This also causes the ejection of low speed fluid from the inner layers to the outer layers.
- They suggested that the Reynolds shear stress is enhanced by this vortex organization mainly due to the stronger low speed flow below the packet of hairpin vortices. Ganapathisubramani et al. (2003) further supported this by showing that the vortex packets in zero pressure gradient boundary layer flow contribute more than 25% to $-\langle u'v' \rangle$ and occupy only 4% of total area.

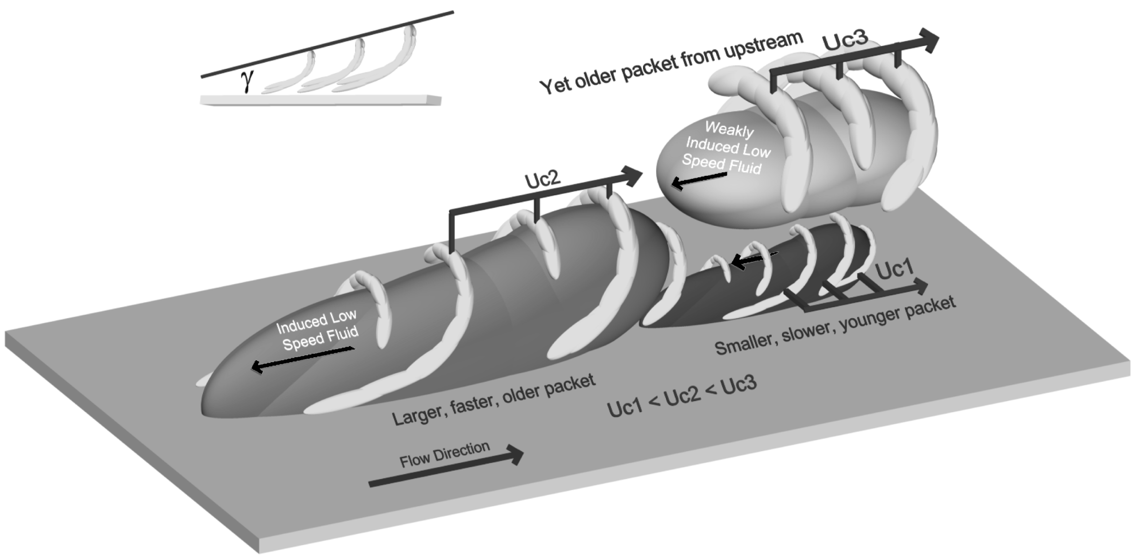

Figure 1.6: Conceptual scenario of hairpins/canes organization in wall bounded turbulent layers (taken from Adrian et al., 2000).

This explains that hairpins are coupled with the low speed streaks in TBL. Papers by Adrian (2007); Elsinga et al. (2010) strengthen the evidence of the organization of hairpin like structures in the outer region. To summarize, the spatial organization of hairpin vortices in a hairpin packet is closely related to $-\langle u'v' \rangle$. Therefore the way in which these structures are organized dynamically and are self-sustaining is deemed relevant in understanding the TBL.

Smith et al. in 1991 proposed an inviscid model to explain the organization of hairpins. They explained how new hairpin vortices are generated from a single hairpin vortex under proper conditions. Furthermore in 1994, Haidari and Smith experimentally proved the generation of new hairpins from a single hairpin vortex in the laminar boundary layer for the first time. This mechanism is also know as auto-generation or parent-offspring concept. Then Zhou et al. (1999) came out with a simple model to explain the mechanisms responsible for auto-generation by numerical simulations of a turbulent boundary layer (channel flow). They investigated these mechanisms by studying the development of an initial condition containing a single, three-dimensional vortex structure called *conditional eddy*. The conditional eddy was extracted by conditional averaging of velocity fields in DNS database of fully turbulent channel flow based on Q2 events. They found that, if the strength (discussed in detail in section 3.2) of an initial condition is above a certain threshold then it auto-generates new hairpin vortices upstream. The robustness of the auto-generation mechanism was demonstrated by Kim, Sung, and Adrian (2008). They followed the same procedure as Zhou et al. (1999) in the calculation of the conditional eddy. They studied the development of this conditional eddy in the presence of added noise or an instantaneous field of turbulent flow. They found auto-generation was robust and that the background noise resulted in reduction of the threshold strength required to trigger auto-generation mainly in the buffer layers.

To summarize in present hairpin model, it has been suggested that the hairpins above certain threshold strength grow from buffer region to outer regions, auto-generate and populate the TBL. But this model still does not completely explain the self sustaining characteristic of flow. Open questions like:

- How does a hairpin vortex of certain threshold strength come into existence?
- Do low speed streaks play any role in auto-generation and if yes, how?

remain unanswered. In this report, question of how a hairpin of certain threshold strength come into existence is addressed. Following possibilities are tested:

- Merging of two hairpin vortices resulting in the formation of a stronger hairpin.
- Interactions between two hairpin vortices leading to auto-generation.

The report is outlined as follows. Chapter 2 defines the aim and approach of the project followed by methodology in chapter 3 where details of numerical methods and extraction of initial condition is described. Validation of the direct numerical simulation code and linear stochastic estimation is covered in chapter 4. Chapter 5 describes observations and results. Finally the conclusions and recommendations are given in chapter 6.

2

PROJECT AIM & APPROACH

The aim of this thesis is *to increase the understanding of hairpin eddy model by studying:*

- *The interaction between two conditional eddies which are aligned perfectly behind each other in stream-wise direction in a TBL.*
- *The role this interaction plays in the auto-generation cycle in a TBL.*

The interaction between two eddies is investigated in different scenarios. These scenarios are created based on initial size and height of the eddy and stream-wise distance between two eddies (Δx). The initial size is determined by initial maximum swirling strength and is discussed in section 3.3. The height of the eddy is defined by the ejection event vector location (y_e^+) which is explained in section 3.2.1. The different scenarios that are investigated are as follows:

1. A small eddy upstream and a large eddy downstream and vice versa with different strength as shown in figure 2.1. Vortices are aligned perfectly behind each other in stream-wise direction.
2. Effect of the stream-wise spacing between vortices. Stream-wise spacing is shown in figure 2.1c. Spacing was constrained due to size of the computational domain and the effect of periodic boundary conditions.

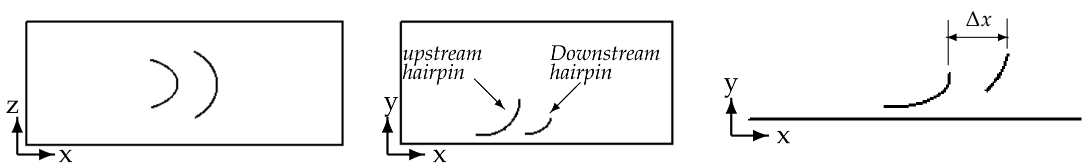

(a) Top view of two vortices aligned in stream-wise direction.

(b) Side view of vortex with higher strength & y_e^+ upstream and lower strength & y_e^+ downstream.

(c) Side view of vortex with higher strength & lower y_e^+ upstream and lower strength & higher y_e^+ downstream with Δx stream-wise spacing.

Figure 2.1: Different scenarios.

Before performing the simulations with two aligned hairpins, the case of a single hairpin vortex was studied. This was done to establish the baseline for analyzing two hairpin cases. In the baseline studies, the initial swirling strength and the height of the hairpin was varied. This variation was studied in terms of maximum swirling strength, mean and maximum ejection events.

APPROACH

All the simulations are performed at low Reynolds number fully turbulent channel flow. A brief summary of the investigation procedure is as follows:

1. Simulation of the fully developed turbulent channel flow is performed using direct numerical simulation at friction Reynolds number (Re_τ)= 360. DNS is discussed in detail in section 3.1. The DNS code is validated by comparing the flow statistics to the paper of Kim et al. (1987) in section 4.1.

2. Paper by Zhou et al. (1999) will be reproduced for single hairpin case to establish the baseline and to validate the procedure and code. Steps followed are:

   a) Initial velocity field containing a single conditional eddy is calculated. It is sum of mean turbulent profile and perturbation velocity field corresponding to conditional eddy extracted from the DNS database. This is explained in section 3.2.

   b) Perturbation velocity field is extracted by conditional averaging (Linear stochastic estimate (LSE)) based on ejection (or Q2) events from the velocity fields obtained in DNS database.

   c) Initial pressure field is calculated by solving the Poisson equation for the pressure.

   d) DNS with the above initial condition to study the evolution and dynamics of the conditional eddy.

   e) Hairpins are visualized by vortex identification method called *swirling strength criterion* which is discussed in detail in section 3.3.

3. After validating the code and procedure, initial condition with two conditional eddies is calculated (see section 3.2).

4. Above mentioned procedure from (c) to (e) will be followed to analyze the evolution of the initial condition containing two eddies.

3

METHODOLOGY

3.1 DIRECT NUMERICAL SIMULATION OF FULLY DEVELOPED CHANNEL FLOW

Direct numerical simulation (DNS) of fully developed channel flow was carried out at friction Reynolds number (Re_τ) $= 360$ (based on full channel height (H)). DNS was done using non-dimensional in-compressible Navier-Stokes equations shown below:

$$\frac{\partial u_i}{\partial x_i} = 0 \tag{3.1}$$

$$\frac{\partial u_i}{\partial t} + u_j \frac{\partial u_i}{\partial x_j} = -\frac{\partial p}{\partial x_i} + \frac{1}{Re_\tau}\frac{\partial^2 u_i}{\partial x_i^2} \tag{3.2}$$

where Re_τ is given by $u_\tau H/\nu$. Non-dimensional scales used in above equations are:

- full channel height (H) for length.
- friction velocity $u_\tau (= \sqrt{\tau_w/\rho})$ for velocity.
- ρu_τ^2 for pressure.
- H/u_τ for time.

Non-dimensionalized computational domain w.r.t H is $2\pi \times 1 \times \frac{2}{3}\pi$ in stream-wise, wall normal and span-wise directions. Boundary conditions employed in simulations were no-slip and no-penetration at wall, periodic in span-wise (z-direction) and stream-wise directions (x-direction). Uniform staggered grids with resolution of $808 \times 128 \times 272$ in x, y and z directions were used.

A pressure-correction method was employed to solve Navier-Stokes equations. In the first step, intermediate velocity based on the convective, diffusive and pressure terms was calculated. This velocity is not divergence free, so in the second step, Poisson equation is solved to obtain correct pressure using intermediate velocity. This corrected pressure is used to obtain the divergence free velocity field. Equations (3.1) and (3.2) were discretized in an explicit way. Runge-Kutta third order scheme was employed for integration in time for advection and diffusion terms. Pressure gradient term was discretized in time using Crank-Nicolson scheme. Central difference was used for spatial derivatives. Details of time integration and spatial discretisation can be found in appendix sections A.1 and A.2.

Initial velocity field to start the DNS was generated from random number function in FORTRAN. Once the flow became fully turbulent, the velocity and pressure data fields were saved. There was good agreement of flow statistics of the present data with the data of Kim et al. (1987). The details of the DNS code validation are discussed in section 4.1. From saved velocity fields, initial condition containing a conditional eddy was extracted.

3.2 INITIAL CONDITION/CONDITIONAL EDDY

The initial condition contains a single conditional eddy or two conditional eddies whose evolution will be studied in detail by DNS. The conditional eddy is a vortex structure extracted from DNS database of fully developed turbulent channel flow as shown in figure 3.1. Velocity field ($\tilde{u}_i(\hat{\mathbf{x}})$) of an initial condition is the sum of turbulent mean profile ($\langle u_i(y)\rangle$) and the perturbation velocities ($\tilde{u}_i'(\hat{\mathbf{x}})$) which correspond to different conditional eddies. It is given by

$$\tilde{u}_i(\hat{\mathbf{x}}) = \tilde{u}_i'(\hat{\mathbf{x}}, \mathbf{E}_1') + \tilde{u}_i'(\hat{\mathbf{x}} + \Delta x, \mathbf{E}_2') + \langle u_i(y)\rangle \tag{3.3}$$

where perturbation velocity $\tilde{u}_i'(\hat{\mathbf{x}}, \mathbf{E}_1')$ corresponds to conditional eddy conditioned to event vector $\mathbf{E}_1'$ and $\tilde{u}_i'(\hat{\mathbf{x}} + \Delta x, \mathbf{E}_2')$ conditioned to event vector $\mathbf{E}_2'$ with stream-wise shift (Δx) from the former. Initial pressure field ($\tilde{p}$) is then calculated using $\tilde{u}_i(\hat{\mathbf{x}})$ by solving the divergence of Navier-Stokes equation as shown below:

$$\frac{\partial}{\partial x_i}\left(\tilde{u}_j \frac{\partial \tilde{u}_i}{\partial x_j}\right) = -\frac{\partial}{\partial x_i}\left(\frac{\partial \tilde{p}}{\partial x_i}\right) \tag{3.4}$$

Perturbation velocities ($\tilde{u}_i'(\hat{\mathbf{x}})$) in equation (3.3) is estimated by conditional averaging of DNS perturbation velocity field (u_i') with respect Q2 events and is given by $\langle u_i'(\hat{\mathbf{x}})|\mathbf{E}'(\mathbf{x}_e)\rangle$. Event $\mathbf{E}'$ is the velocity event defined at point $\mathbf{x}_e$ conditioned to occurrence of Q2 events. Conditional average $\langle u_i'(\hat{\mathbf{x}})|\mathbf{E}'(\mathbf{x}_e)\rangle$ is a non-linear function of events $\mathbf{E}'$ which makes it complex and difficult to compute. Hence it is estimated linearly as a function of $\mathbf{E}'$. And this procedure is called as Linear stochastic estimate (LSE).

3.2.1 *Linear Stochastic Estimate (LSE)*

This procedure has been extensively discussed in Adrian (1994, 1996). LSE is linear estimate of conditional averaging and is given by

$$\begin{aligned}
\tilde{u}_i{}'(\hat{\mathbf{x}}) &= \text{Linear estimate of} \langle u_i'(\hat{\mathbf{x}})|\mathbf{E}'(\mathbf{x}_e)\rangle && (3.5)\\
&= \text{Linear estimate of} \langle u_i'(x_e + r_x, y, z_e + r_z)|\mathbf{E}'(x_e, y_e, z_e)\rangle && (3.6)\\
&= \sum_{j=1}^{3} L_{ij}(\hat{\mathbf{x}}, \mathbf{x}_e) E_j' && (3.7)
\end{aligned}$$

where L_{ij} are linear estimate coefficients. L_{ij} is chosen such that the mean square error between conditional averaging $\langle u_i'(\hat{\mathbf{x}})|\mathbf{E}'(\mathbf{x}_e)\rangle$ and LSE ($\tilde{u}_i'$) is minimum.

$$\left\langle \left[\langle u_i'(\hat{\mathbf{x}})|\mathbf{E}'(\mathbf{x}_e)\rangle - \sum_j L_{ij} E_j'\right]^2 \right\rangle = \text{minimum} \tag{3.8}$$

Minimization of the above condition yields to the Yule-Walker equations given by

$$\sum_j \langle E_j'(\mathbf{x}_e) E_k'(\mathbf{x}_e)\rangle L_{ij} = \langle E_k'(\mathbf{x}_e) u_i'(\hat{\mathbf{x}})\rangle \qquad k = 1, 2, 3 \tag{3.9}$$

$\langle E_j' E_k'\rangle$ and $\langle E_k' u_i'\rangle$ represent the two-point correlations between event vector with event vector and event vector with velocity field respectively. Events $E_j'(\mathbf{x}_e)$ and $E_k'(\mathbf{x}_e)$ in equation (3.9) are perturbation velocity values at plane y_e. The value of event vector E_j' in equation (3.5) is defined at a point and is based on second quadrant(Q2) events $u' < 0$, $v' > 0$.

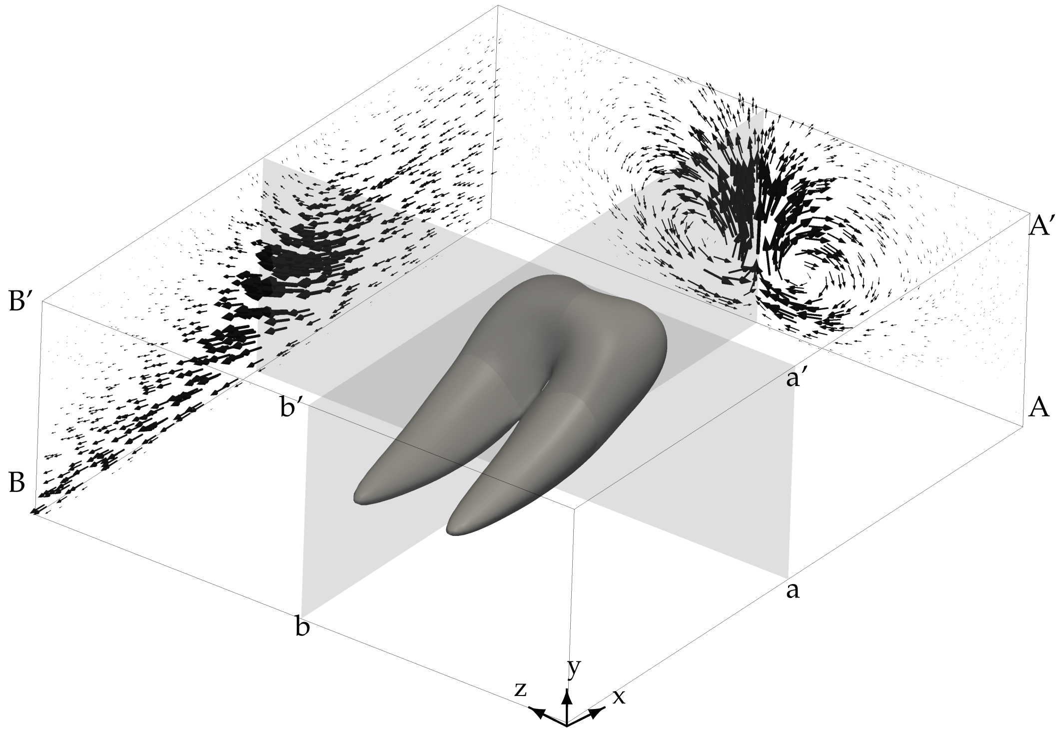

Figure 3.1: Initial condition showing conditional eddy for $y_e^+ = 68.4$ and $\alpha = 2$. Conditional eddy is iso-surface of $\lambda_{ci}^2 = 33$, which is 5% of maximum λ_{ci}^2. Vector plots correspond to in plane perturbation velocities. Vector plot on plane aa' and bb' is translated to plane AA' and BB' respectively for better visualization.

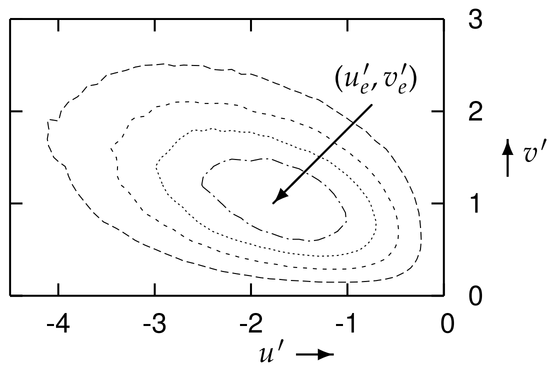

Figure 3.2: Second quadrant: Contours of weighted Reynolds shear stress $(-u'v'f_{uv})$. u'_e and v'_e represent velocity values which maximize contribution to Reynolds shear stress at $y_e^+ = 103$ in a turbulent plane channel flow.

It is given by $(\alpha u'_e, \alpha v'_e, \alpha w'_e)$. The multiplicative factor α represents the relative strength of a conditional eddy. For symmetric Q2 events, $w'_e = 0$ and $w'_e \neq 0$ for asymmetric case. (u'_e, v'_e) corresponds to a value that has maximum contribution to Reynolds shear stress $-\langle u'v' \rangle$ in quadrant 2 for given y_e as shown in figure 3.2. This is obtained from the product of $f_{uv}(u', v')$ with $u'v'$ where $f_{uv}(u', v')$ represents joint probability density function of occurrence of u' and v'. It is observed (see Zhou et al., 1999) that the relative amplitude α plays an important role in auto-generation for a given y_e.

3.3 VORTEX IDENTIFICATION

One of the main aspects of the present study is the identification and tracking of vortices. In present case, vortex identification is based on the local swirling strength suggested by Zhou et al. (1999). Local swirling strength is defined as imaginary part(λ_{ci}) of a complex eigenvalue of a velocity gradient tensor. If the eigenvalues are real then local swirling strength is zero. Subscripts c and i in λ_{ci}, represent complex number and imaginary part respectively. Velocity gradient tensor $\mathcal{D}_{ij}$ is given by

$$\mathcal{D}_{ij} = \frac{\partial u_i}{\partial x_j} \tag{3.10}$$

and in present case it is calculated as shown in appendix section A.3 on page 35. Vortices are identified by plotting the iso-surfaces of λ_{ci}^2. Initial condition containing conditional eddy visualized by local swirling strength criterion is shown in figure 3.1.

4

VALIDATION

The procedure and code used in the present simulations is validated in three steps. In section 4.1, the DNS code is validated. The linear stochastic estimate procedure for generating the initial conditional eddy and vortex identification method are compared and verified in section 4.2. The periodic boundary effect in the stream-wise direction is studied in the last section 4.3.

4.1 DNS SIMULATIONS

The employed DNS code was validated by comparing the present turbulent flow statistics to the data in the paper of Kim et al. (1987) at comparable Reynolds number.

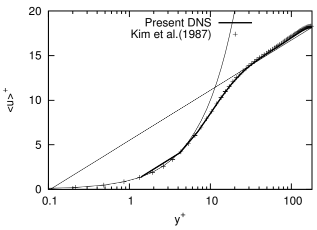

(a) Mean velocity comparison.

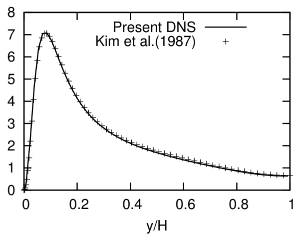

(b) u_{rms} velocity comparison.

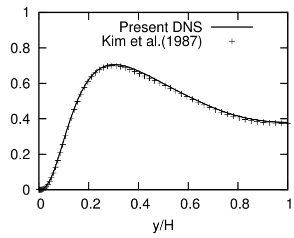

(c) v_{rms} velocity comparison.

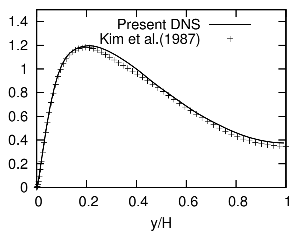

(d) w_{rms} velocity comparison.

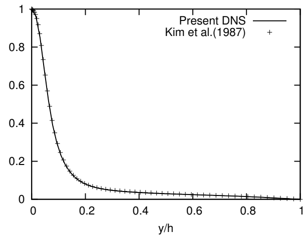

(e) Mean shear stress comparison.

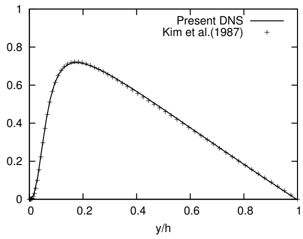

(f) Reynolds shear stress comparison.

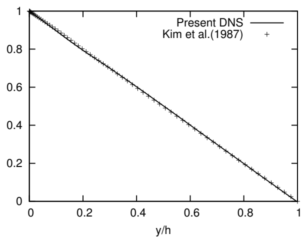

(g) Total shear stress comparison.

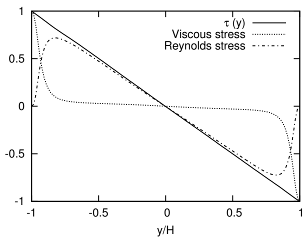

(h) Shear stress of present data.

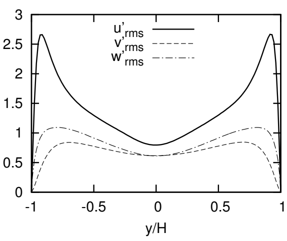

(i) rms velocities of present data.

Figure 4.1: Comparison and validation of present DNS with data of Kim et al. (1987).

Comparison of the mean stream-wise velocity, the rms velocities and the shear stress can be seen in figure 4.1. Reynolds number and friction coefficient based on mean center line velocity($\langle u_c \rangle$) and bulk velocity(u_b) are shown in table 4.1. The value of the bulk Reynolds number reported in the present case is slightly higher than the one reported in Kim et al.. This very small difference is due to the difference in Re_τ which is 360 in the present case and 356.24 in Kim et al.. Even though Re_τ is slightly higher in the present case, the bulk velocity is smaller presumably because of the diffusive nature of the numerical scheme compared to the one used in Kim et al..

Variable	Present	Kim et al. (1987)	Variable	Present	Kim et al. (1987)
$Re_c = \frac{\langle u \rangle_c h}{\nu}$	3276	3300	$Re_b = \frac{u_b H}{\nu}$	5612	5600
u_b/u_τ	15.589	15.63	$\langle u_c \rangle/u_\tau$	18.165	18.20
$c_f = \frac{\tau_w}{\frac{1}{2}\rho u_b^2}$	8.23×10^{-3}	8.18×10^{-3}	$c_{fo} = \frac{\tau_w}{\frac{1}{2}\rho \langle u \rangle_c^2}$	6.06×10^{-3}	6.04×10^{-3}

Table 4.1: Comparison of mean flow variables.

Both in figure 4.1 and table 4.1, it can be observed that there is a very good agreement between the simulations, which validates present DNS simulations.

4.2 LINEAR STOCHASTIC ESTIMATE AND VORTEX IDENTIFICATION

The validation of the linear stochastic estimate and the vortex identification procedure is done by comparing the maximum of the square of swirling strength (λ_{ci}^2) and geometric shape of the resulting conditional eddy structure against Zhou et al. (1999). Perturbation velocity fields representing the conditional eddy were calculated for different relative strength of a conditional eddy (α) using the linear estimate coefficients (L_{ij}) evaluated at three different event vector locations namely $y_e^+ = 46.4, 68.9, 102.7$ as described in section 3.2.1. Then the swirling strength (λ_{ci}) was evaluated from the perturbation velocities as explained in section 3.3.

y_e^+	$\lambda_{ci}^2(\alpha = 3)$	$\lambda_{ci}(\alpha = 1) = \sqrt{\frac{\lambda_{ci}^2(\alpha)}{\alpha^2}}$
102.7	765.22	9.22
68.9	1525.55	13.02
46.4	3151.08	18.71

Table 4.2: Swirling strength at different α and y_e^+ in present case.

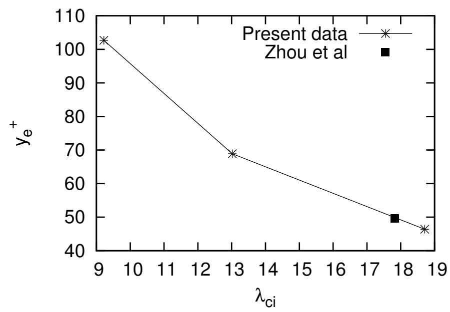

Figure 4.2: λ_{ci} non-dimensionalized w.r.t u_τ/H at $\alpha = 1$ vs y_e^+.

Table 4.2 shows the values of swirling strength λ_{ci} (non-dimensionalized by u_τ/H) in the present case. Zhou et al. (1999) reported the value of λ_{ci}^2 (λ_{ci} non-dimensionalized by u_τ/h) at $(y_e^+, \alpha) = (49.6, 3)$ to be 715. This is equivalent to $\lambda_{ci} = 8.913$ at relative strength $\alpha = 1$. In the present case swirling strength (λ_{ci}) is twice the value reported by Zhou et al. as the non-dimensional length scale used in present case is full channel height(H) compared to half channel height(h) in Zhou et al.. The value of λ_{ci} reported by Zhou et al. shows a good agreement with the present data as it fits into the trend of increasing λ_{ci} with decreasing y_e^+ as shown in figure 4.2.

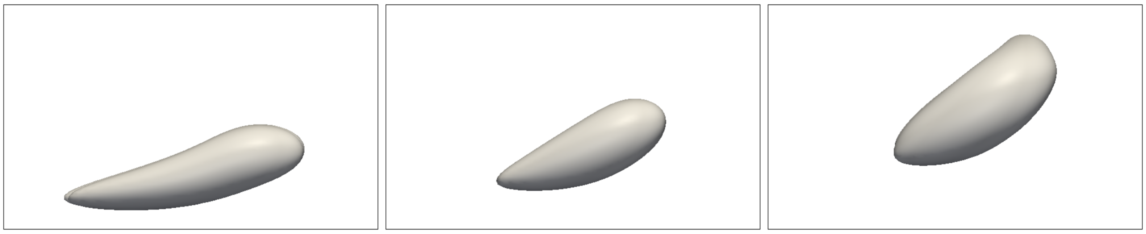

(a) Side view. From left to right $y_e^+ = 46.4,\ 68.9,\ 102.7$.

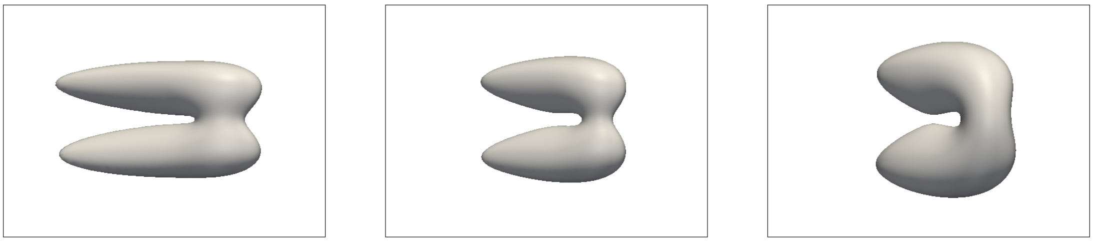

(b) Top view. From left to right $y_e^+ = 46.4,\ 68.9,\ 102.7$.

Figure 4.3: Initial conditional eddies with same(approx) maximum $\lambda_{ci}^2 = 350$ but with different ejection event location (y_e^+). Iso-surfaces correspond to 10% of max λ_{ci}^2.

The geometric shape of the initial conditional eddies is shown in figure 4.3. Some notable features are:

- The inclination angle of the eddy decreases as the event vector location y_e^+ is decreased.
- The span-wise separation of legs at upstream end of the eddy is about 100 wall units irrespective of the y_e^+ at this low Reynolds number.

These observations are consistent with the ones reported in the papers of Zhou et al. (1999) and Kim et al. (2008).

4.3 PERIODIC BOUNDARY EFFECTS ON THE GENERATION OF HAIRPINS

The effect on the simulations due to periodic boundary condition in the stream-wise direction was studied based on the evolution of the conditional eddy $(y_e^+, \alpha) = (68.9, 2)$. The simulation was carried out on the original and a larger computational domain with the stream-wise length thrice the original stream-wise length. The perturbation velocity field corresponding to the conditional eddy was calculated for the original domain by LSE. In the original do-

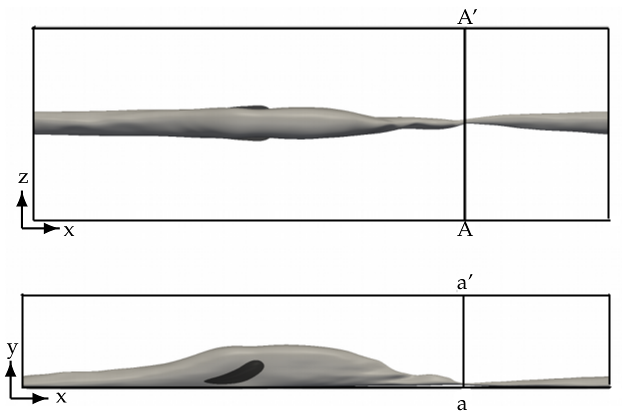

Figure 4.4: Selection of boundary in original domain for creating the initial condition for large domain. Black contour indicates eddy and gray indicates low speed streak contour $u' < 0.1$. Top view and side view of the channel are top and bottom pictures respectively.

main, a yz-plane with lowest perturbation velocities values (plane AA' and aa' in figure 4.4) was located and shifted to the boundary in original domain. This shifted perturbation velocity field was used as the initial condition in the large domain as shown in figure 4.5.

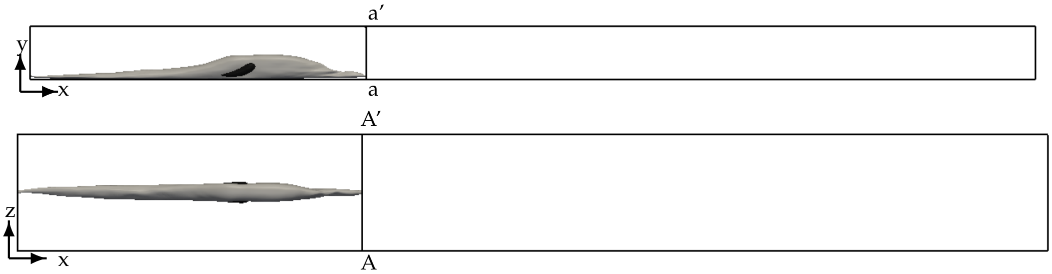

Figure 4.5: Initial condition in the large-domain. yz-planes (aa′, AA′) are same as the ones in the original domain shown in figure 4.4. Black contour indicates eddy and gray indicates low speed streak contour $u' < 0.1$. Side view and top view of the channel are top and bottom pictures respectively.

Simulations were carried out to analyze the evolution of the initial structure. Figures 4.6a and 4.6b represents the variation of the normalized maximum λ_{ci}^2 and normalized maximum $-u'v'$ where $u' < 0, v' > 0$ (ejection event). It can be noticed that the values in both the domains agree perfectly. The geometric shapes of the evolution of conditional eddy with time also looked similar in both the cases. From these observations it is concluded that there is no significant effect of the periodic boundary on the original domain. Hence it is considered sufficient by long for the present simulations.

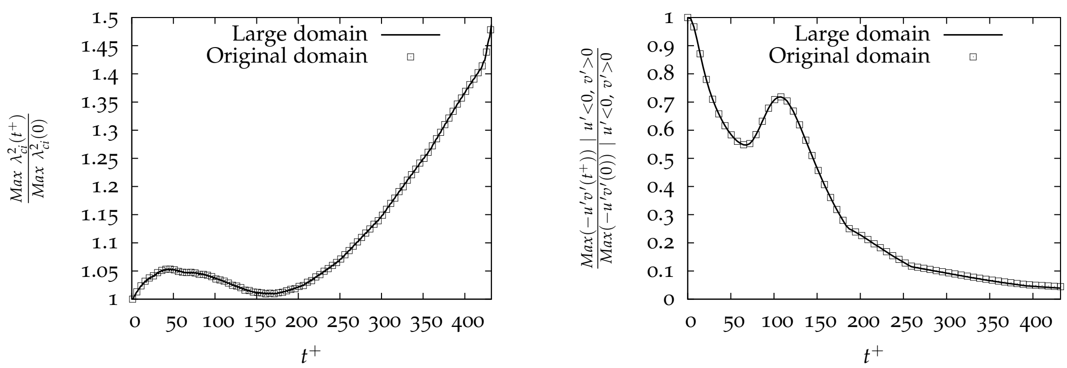

(a) Normalized maximum of the square of swirling strength (λ_{ci}^2).

(b) Normalized maximum of $-u'v' \mid u' < 0,\ v' > 0$ ejection events.

Figure 4.6: Comparison of the original and large computational domain.

To summarize, comparison of statistical data obtained from DNS, LSE and vortex identification codes shows a very good agreement with the data given in literature. Hence the codes are considered sufficiently robust for simulating and analysis of initial condition with two eddies.

5

RESULTS

Simulations of the initial condition with a single eddy case will be discussed before considering the cases in which the initial flow contains two eddies. This is done in-order to establish the base-line for later comparison. In this report, the observations and mechanisms of evolution of the initial conditions with single eddy are validated by comparing results with the papers of Zhou et al. (1999) and Kim et al. (2008). The dynamics of evolution of the single eddy is briefly explained in the appendix B and more details can be found in the papers of Zhou et al. (1999) and Kim et al. (2008).

For the initial condition with two eddies, it is studied:

- if merging is possible or not.
- if interaction between two eddies leads to stronger eddies and or the generation of new structures (auto-generation).

The development of the 3-dimensional eddy is quantified in terms of its peak swirling strength (λ_{ci}), maximum of $-u'v'$ where $u' < 0, v' > 0$ (ejection event) and volume average of $-u'v'$ where $u' < 0, v' > 0$.

5.1 SIMULATIONS WITH SINGLE CONDITIONAL EDDY

y_e^+	α	Max λ_{ci}^2	Auto-generation
46.4	1.0	350.12	No
46.4	3.0	3151.08	Yes
68.9	1.0	169.51	No
68.9	1.2	244.09	No
68.9	1.4	332.23	No
68.9	1.6	433.94	No
68.9	1.8	549.20	No
68.9	2.0	678.02	Yes
102.7	1.0	85.02	No
102.7	2.0	340.1	No
102.7	3.0	765.2	Yes

Table 5.1: Characteristics of the individual hairpin simulations.

The simulation of the different initial conditions containing only a single conditional eddy are listed in table 5.1. The conditional eddy in the initial condition is a pair of lifted, counter-rotating stream-wise vortices. It evolves into a hairpin vortex which is referred as primary hairpin (Zhou et al., 1999). The dynamics of the evolution of an eddy into a primary hairpin is discussed in appendix section B.1. It was observed that the individual conditional eddies shown in table 5.1, evolve into a primary hairpin vortex. The mechanisms responsible for the evolution of the conditional eddy into a primary hairpin is same in all the cases. From this it may be inferred that these mechanisms must be similar for the evolution of any lifted, counter-rotating stream-wise vortices. From Zhou et al. (1999) and present observations, few of the important points connected with the evolution of an eddy into a hairpin and its further development are as follows:

- A conditional eddy based on lower y_e^+, evolves slower into a hairpin as the shear layer roll up into a span-wise vortex is delayed due to the lower mean flow velocity. Shear layer is formed when ejected fluid between stream-wise legs encounters the mean flow.

- Increasing α results in higher initial swirling strength, which leads to faster development of stream-wise vortices into a hairpin. This is due to intense shear layer formation in between the legs and top of the stream-wise vortices.

Few additional observations were made in the present simulations. They are:

- A conditional eddy with higher swirling strength (or higher relative strength α) travels at the same speed or slightly slower than a weaker eddy at the same event location (y_e^+) as shown in figure B.4 and figure B.5 on page 41.

- A conditional eddy based on an event specified at higher event vector location (y_e^+) travels faster for the same swirling strength as shown in figure B.6 on page 41.

In the following section, the 4-dimensional (x, y, z, t) observations are quantified in 2-dimensional form (λ_{ci}, t), or $(-u'v', t)$ as shown in figure 5.1 for the ease of analysis.

5.1.1 *2-dimensional signature of 4-dimensional data*

Figure 5.1a shows the normalized maximum of the square of swirling strength $(\max \lambda_{ci}^2)$ for event vector location $y_e^+ = 102.7$. The value of the max λ_{ci}^2 increases with the initial strength α. This is also observed in the case of $y_e^+ = 68.9$ as shown in figure B.7 on page 42.

In figure 5.1a, for the relative strength $\alpha = 3$, the value of the max λ_{ci}^2 increases to a maximum and then decreases to a local minimum at $t^+ = 111.6$. At the same time, the wall normal location of the max λ_{ci}^2 increases from $y^+ = 97$ at $t^+ = 0$ to $y^+ = 215$ at $t^+ = 83$ and then decreases to $y^+ = 190$ at $t^+ = 111.6$. This can be observed in the figure 5.1b. The stream-wise location of the max λ_{ci}^2 travels in downstream direction linearly with time till $t^+ = 111.6$ as shown in figure 5.1c. Initially the location of the max λ_{ci}^2 corresponds to the region of the downstream part of the quasi-stream-wise vortices of the conditional eddy at $t^+ = 0$, which evolves into a head of the hairpin till $t^+ = 111.6$. After $t^+ = 111.6$, the location of the max λ_{ci}^2 decreases to $y^+ = 60$ at $t^+ = 116$ (see figure 5.1b) and also the stream-wise location of the max λ_{ci}^2 shifts upstream relative to the hairpin head (see figure 5.1c). This new location corresponds to the region of the stream-wise vortex legs. The swirling strength of these vortex legs keeps increasing from $t^+ = 0$ and at $t^+ = 116$, it becomes more than the swirling strength (λ_{ci}) present in the head. After $t^+ = 116$, for $\alpha = 3$, it can be seen that the max λ_{ci}^2 continues to increase, goes to a maximum and then decreases. Around the same time, new structures begin to evolve.

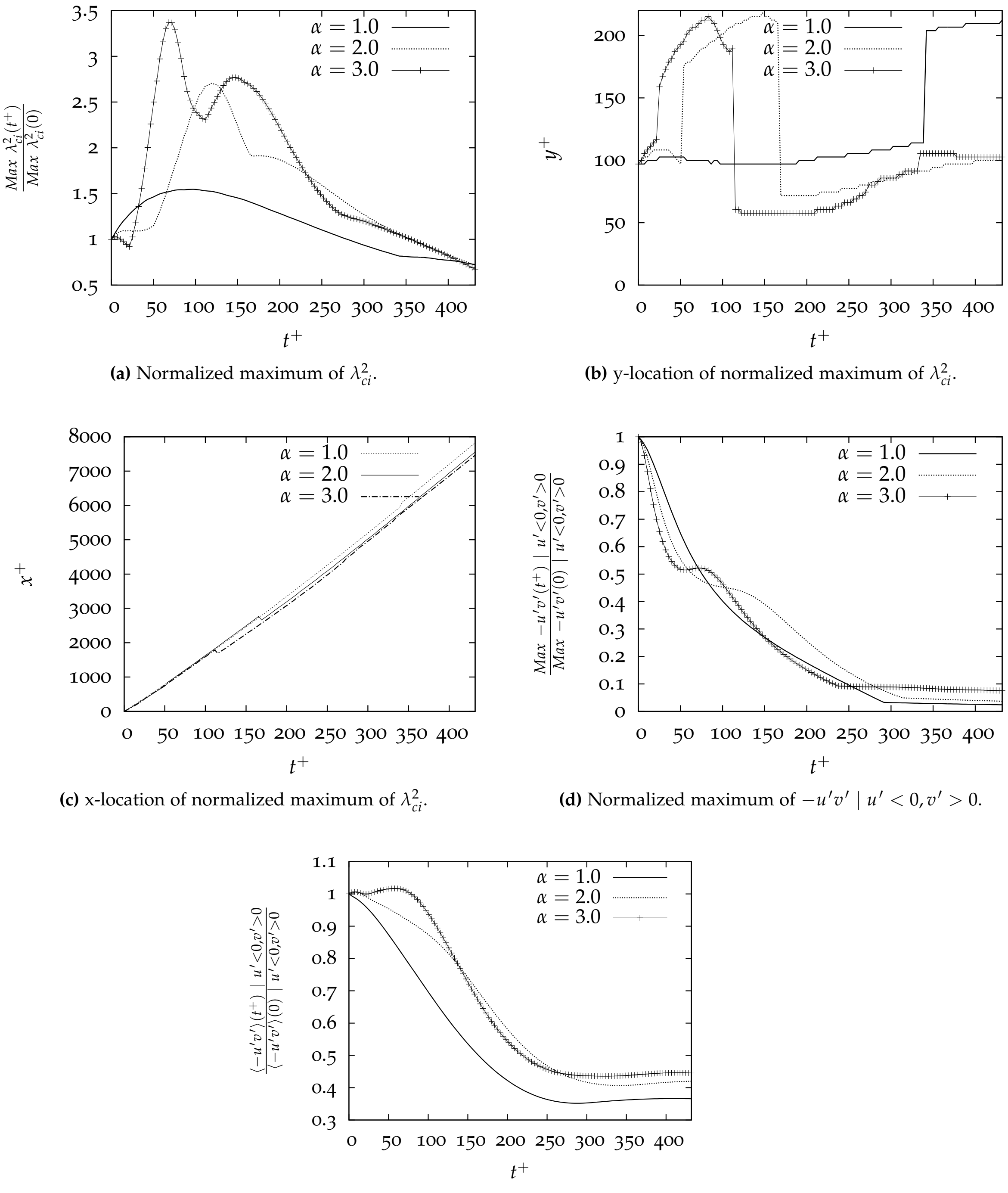

(a) Normalized maximum of λ_{ci}^2.

(b) y-location of normalized maximum of λ_{ci}^2.

(c) x-location of normalized maximum of λ_{ci}^2.

(d) Normalized maximum of $-u'v' \mid u' < 0, v' > 0$.

(e) Normalized volume average $-u'v' \mid u' < 0, v' > 0$.

Figure 5.1: Temporal evolution of (a) Normalized maximum of the square of swirling strength (λ_{ci}^2). (b) wall-normal location (y^+) of the normalized maximum λ_{ci}^2. (c) Stream-wise location (x^+) of the normalized maximum λ_{ci}^2. (d) Normalized maximum of Reynolds shear stress $-u'v'$ where $u' < 0, v' > 0$ (ejection event). (e) Normalized volume average of Reynolds shear stress $(-\langle u'v' \rangle$ where $u' < 0, v' > 0)$. for single initial eddy at $y_e^+ = 102.7$. All values are normalized with their initial value at $t^+ = 0$.

For $\alpha = 2$, till $t^+ = 165.6$, the location of the max λ_{ci}^2 corresponds to the head and then shifts to the stream-wise vortex legs. After $t^+ = 165.6$, the max λ_{ci}^2 increases a little and then decreases. But no new structures are formed. For $\alpha = 1$, the location of the max λ_{ci}^2

corresponds to the head. These observations can be correlated with the 3-d evolution of an eddy as follows:

- Initially the maximum of the square of swirling strength (λ_{ci}^2) increases faster for the case of relative strength $\alpha = 3$ compared to $\alpha = 2$ and is present in the region which evolves into the head. This also can be explained as the initial growth rate (variation of max λ_{ci}^2 with respect to time) is higher in the case of $\alpha = 3$ than $\alpha = 2$. This is associated with the evolution of an initial eddy into a primary hairpin which is mainly the formation of the head. The evolution of the primary hairpin is faster in case of $\alpha = 3$ compared to $\alpha = 2$. For $\alpha = 1$, primary hairpin evolves slower than in $\alpha = 2$ which can also be observed in figure 5.1a.

- The growth rate of max λ_{ci}^2 in the stream-wise vortex legs after $t^+ = 111.6$ for $\alpha = 3$, is much higher then the case of $\alpha = 2$ after $t^+ = 165.6$. New structures evolve in the case of $\alpha = 3$ and no new structures for $\alpha = 2$ case. So the higher growth rate in the stream-wise vortex legs may be associated with the generation of new structures because the new structures are resulting from an instability in the legs (Zhou et al., 1999).

In case of the initial condition with $y_e^+ = 68.9$ (see figure B.7a on page 42), the max λ_{ci}^2 for $\alpha = 2$ does not have the same trend as explained above for $y_e^+ = 102.7$. The location of max λ_{ci}^2 stays in the head for longer time ($t^+ = 256$) and it auto-generation occurs around $t^+ = 220$. So by the time, the location of the max λ_{ci}^2 shifts to the stream-wise vortex legs the auto-generation has already occurred and the max λ_{ci}^2 is decreasing in the vortex legs. So it is important to have the plots of the max λ_{ci}^2 and its location for proper interpretation.

The volume average[1] of $-u'v'$ where $u' < 0, v' > 0$ normalized with the initial volume average at $t^+ = 0$ is shown in figure 5.1e. In the figure, for $\alpha = 3$, it can be observed that the volume average slightly decreases in the beginning and then increases. After reaching maximum it decreases continuously and for $\alpha = 1,\ 2$ it always decreases. For the case of $y_e^+ = 68.9$ shown in figure B.7c on page 42, the normalized volume average of $-u'v'$ where $u' < 0, v' > 0$ increases with α. So in general, these figures show that the amount of volume averaged Reynolds shear stress due to the ejection events increases with α.

The maximum of $-u'v'$ where $u' < 0, v' > 0$ normalized with the initial maximum at $t^+ = 0$ is shown in figure 5.1d for $y_e^+ = 102.7$ and figure B.7b on page 42 for $y_e^+ = 68.9$. The maximum $-u'v'$ for $\alpha = 3$ decreases at first then slightly increases and reaches a maximum at $t^+ = 72$. After that it again decreases. The normalized maximum $-u'v'$ for event vector location $y_e^+ = 68.9$ shows the same trend as $y_e^+ = 102.7$ and is shown in B.7b.

The time of occurrence of peaks in the max λ_{ci}^2, maximum $-u'v'$ and volume averaged $-u'v'$ (or $-\langle u'v' \rangle$) is shown in table 5.2. It can be seen that the max λ_{ci}^2 and the maximum $-u'v'$ occur at approximately the same time. There is difference in time of about 3.6 units which happens to be the time step at which these values are calculated. From the table 5.2, it is observed that the $-\langle u'v' \rangle$ lags the max λ_{ci}^2 and the maximum $-u'v'$ for all cases except $(y_e^+, \alpha) = (68.9, 2)$. These trends can be clearly observed in the figures.

1 Sum of $-u'v'$ when $u' < 0, v' > 0$ at all the points in the computational domain divided by total number of points in the computational domain

y_e^+	α	t^+ of peak max λ_{ci}^2	t^+ of peak max $-u'v'$	t^+ of peak $-\langle u'v' \rangle$
102.7	3	68.4	72	57.6
68.9	2	104.4	104.4	108
68.9	1.8	126	122.4	118.8
68.9	1.6	147.6	144	126

Table 5.2: Time of occurrence of peaks in maximum λ_{ci}^2, maximum $-u'v'$ and $-\langle u'v' \rangle$ from figure 5.1 and B.7.

5.2 SIMULATIONS OF INITIAL CONDITION WITH TWO EDDIES

Table 5.3 briefly summarizes all the two eddy cases that were studied in this thesis project. In table 5.3, *Ref Plane* refers to event vector location where y_{e1}^+ refers to the upstream eddy and y_{e2}^+ to the downstream eddy. In all the simulations, event vector locations $y_e^+ = 102.7,\ 68.9$ were used. Strength (α_1, α_2) is the initial strength of an eddy where α_1 corresponds to the upstream eddy and α_2 to the downstream eddy. Only $\alpha = 2$ for $y_e^+ = 68.9$ can auto-generate new structures when simulated as a single eddy case. All others do not auto-generate when simulated as single eddies. The stream-wise separation distance (Δx^+) is the distance between two eddies in stream-wise direction in wall units. *Position (y/H)* is the wall-normal location of maximum λ_{ci}^2. It can be noticed that almost all the cases auto-generate except two. Criteria for deciding if merging occurs or not is done by visual inspection. Merging of eddies for $\Delta x^+ = 70.3$ is not applicable. This is because the initial eddies have almost merged, which can be seen in figure 5.2 for different λ_{ci}^2. Whether merging is possible or not in the other cases and how it happens is explained in the next section.

Case	Ref Plane (y_{e1}^+, y_{e2}^+)	Strength $(\alpha_1,\ \alpha_2)$	Δx^+	Max λ_{ci}^2	Position (y/H)	Auto-generation	Merging
I	102.7_68.9	2_1	70.3	331.36	0.2617	Yes	NA
I	102.7_68.9	2_1	101	328.08	0.2695	Yes	Yes
I	102.7_68.9	2_1	140.6	333.75	0.2695	Yes	Yes
I	102.7_68.9	2_1	281.2	336.12	0.2695	Yes	No
I	102.7_68.9	2_1	421.9	343.06	0.2695	No	No
II	102.7_68.9	1_2	70.3	690.37	0.1758	Yes	NA
II	102.7_68.9	1_2	140.6	688.10	0.1758	Yes	Yes
III	68.9_102.7	2_1	140.6	738.52	0.1758	Yes	No
III	68.9_102.7	2_1	281.2	691.15	0.1758	Yes	No
IV	68.9_102.7	1_2	140.6	371.37	0.2617	Yes	No
IV	68.9_102.7	1_2	281.2	348.14	0.2695	No	No

Table 5.3: Overview of simulations of the cases with two eddies.

5.3 MERGING OF HAIRPINS

From table 5.3, it can be seen that merging is observed for the cases with a large upstream and a smaller downstream eddy (Case I and II). Large eddy is calculated at the higher

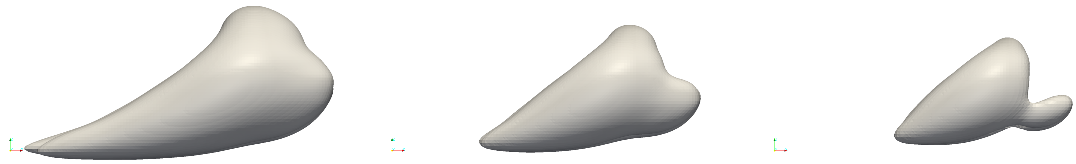

Figure 5.2: Initial flow structure of Case I $\Delta x = 70.3$ showing $\lambda_{ci}^2 = 30,\ 60,\ 90$ surfaces.

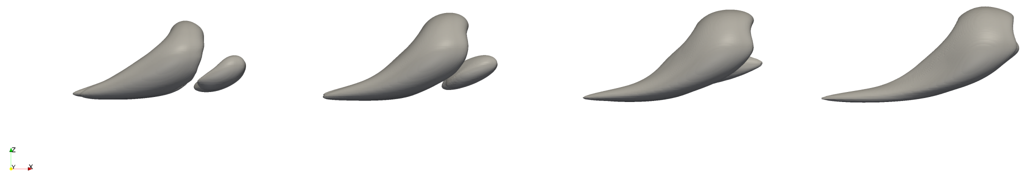

(a) Case I, $\Delta x^+ = 101$. At time (from left to right) $t^+ = 0,\ 14.4,\ 28.8,\ 43.2$.

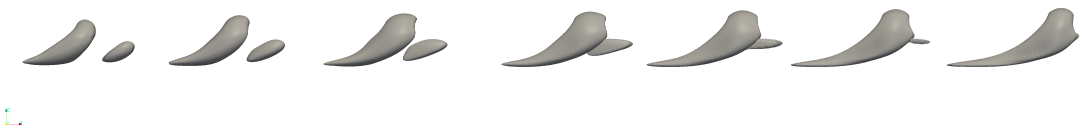

(b) Case I, $\Delta x^+ = 140.6$ At time (from left to right) $t^+ = 0,\ 14.4,\ 28.8,\ 43.2,\ 50.4,\ 57.6,\ 64.8$.

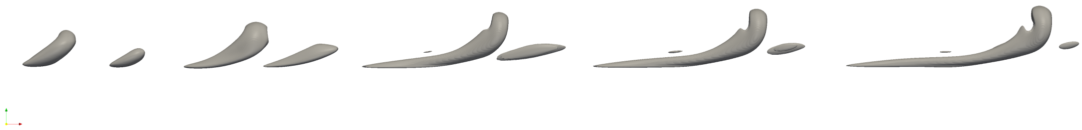

(c) Case I, $\Delta x^+ = 281.2$ At time (from left to right) $t^+ = 0,\ 57.6,\ 129.6,\ 158.4,\ 194.4$.

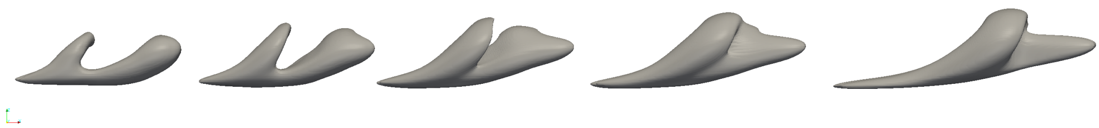

(d) Case II, $\Delta x^+ = 140.6$ At time (from left to right) $t^+ = 0,\ 14.4,\ 28.8,\ 36.0,\ 50.4$.

Figure 5.3: Merging of eddies with different initial spacing (fig $a - c$) and strength (fig d). Side view of 3-d vortices in xy plane. All vortices are visualized by iso-contours of $\lambda_{ci}^2 = 30$.

ejection event location. The small eddy is calculated at lower ejection event location relative to location of the large eddy. Cases III and IV with a small eddy upstream and a large downstream, do not show any signs of merging. In case III and IV, the large downstream eddy moves faster than the small upstream eddy, because an eddy with the higher y_e^+ travels faster then the lower y_e^+ due to higher mean flow velocity as explained in section 5.1. The reverse also happens, the larger eddy upstream travels faster and catches up with the smaller eddy downstream till it merges. Such a scenario has been observed experimentally in a turbulent boundary layer by Elsinga et al. (2012). Merging is studied further as a function of the stream-wise spacing and the strength.

5.3.1 *Merging as function of spacing*

Merging as function of spacing is studied for case I, where the strength of the large eddy upstream was higher than the smaller eddy downstream. From table 5.3 and figures 5.3a, 5.3b and 5.3c, it can be observed that merging occurs when the two eddies are separated by stream-wise distance $\Delta x^+ < 140.6$. For the cases with stream-wise spacing $\Delta x^+ = 281.2$ & 421.9, there is no merging. For the stream-wise separation $\Delta x^+ = 140.6$ (see figure 5.3b), merging is happening, and at the same time the strength of the downstream eddy is reducing (nearly vanishing). This maybe due to the influence of the stronger upstream eddy. The stronger upstream eddy pulls the downstream eddy towards itself. This leads to thinning and stretching of downstream eddy which can be observed in the movie attached.

5.3.2 *Merging as function of strength*

Stream-wise spacing was fixed and the strength of the eddies was varied. Case I and case II with same stream-wise spacing $\Delta x^+ = 140.6$ between eddies was considered. In case II, there was a quicker and clearer merging of the two eddies. Unlike the case I, the strength of the downstream eddy does not strongly reduce in case II. Based on this observation and that of the case I with $\Delta x^+ = 140.6$, it can be inferred that the distance between the eddies may be more then $\Delta x^+ = 140.6$ for merging to occur in case II. In case II, the downstream eddy is stronger (compared to case I), hence it takes more time before its strength diminishes allowing merger over a longer period (i.e, larger separation distance). The eddies are pulled closer to each other much faster in case II where the downstream eddy is stronger. The amount of fluid pumped between the legs of an eddy increases with strength. So the faster approach of the eddies is due to the absorption of fluid by the upstream eddy from the downstream eddy.

To summarize the above two sections:

- There is certain distance between the eddies within which a merger can occur like $\Delta x^+ < 140$ in case I.
- Merging is also dependent on the strength of eddies. It is faster when the strength of the smaller downstream eddy is higher.
- After merging the geometric shape of the structure remains broadly similar (i.e, hairpin-like see figure 5.3a at $t^+ = 43.2$).

5.4 IS AUTO-GENERATION POSSIBLE WHEN TWO EDDIES ALIGN?

In this section, we study if auto-generation can occur or not when two eddies are aligned in the stream-wise direction. Auto-generation described in Zhou et al. (1999) means generation of new hairpin vortices from a parent hairpin vortex. In the present case, auto-generation is loosely referred to as the creation of new structures whether hairpins or pair of counter-rotating quasi-stream-wise vortices.

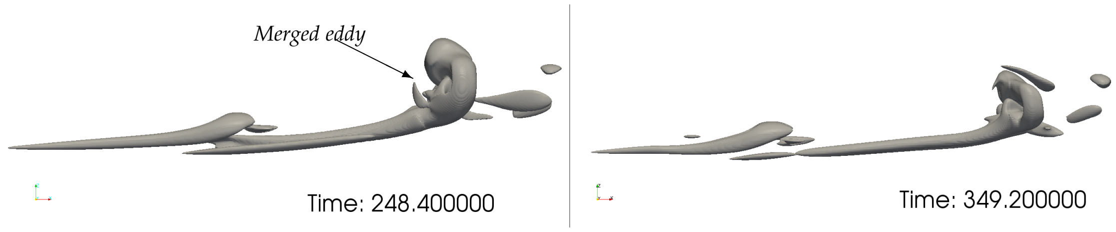

(a) Case I with $\Delta x^+ = 70.3$.

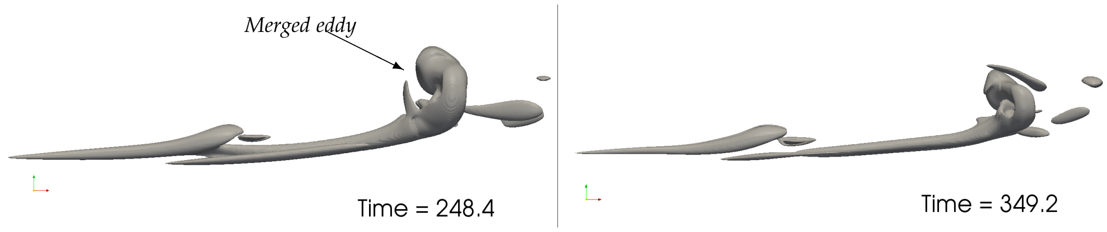

(b) Case I with $\Delta x^+ = 101$.

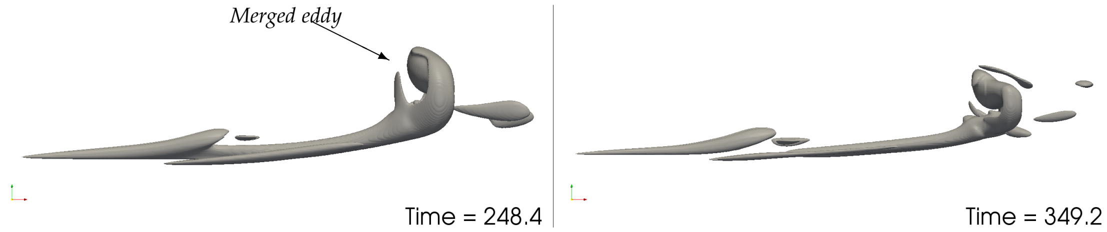

(c) Case I with $\Delta x^+ = 140.6$.

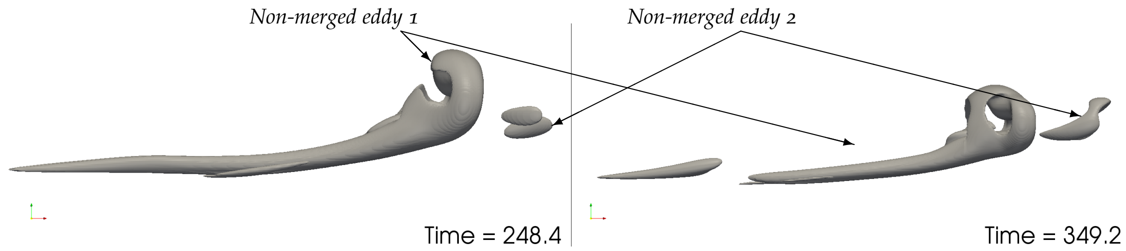

(d) Case I with $\Delta x^+ = 281.2$.

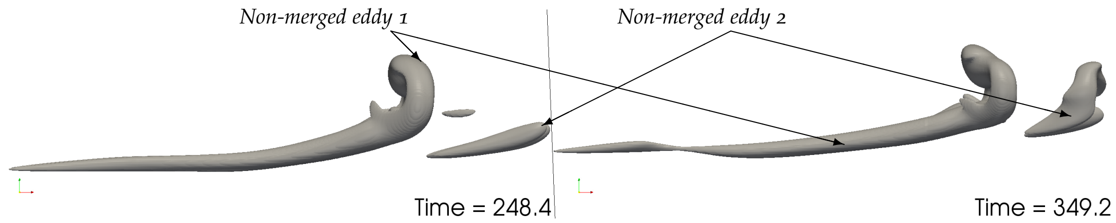

(e) Case I with $\Delta x^+ = 421.9$.

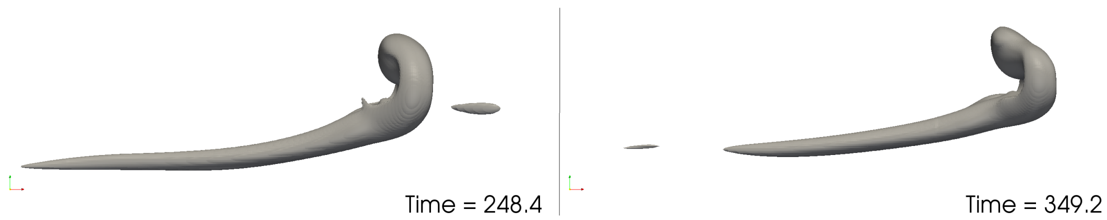

(f) Simulation of single eddy $(y_e^+, \alpha) = (102.7, 2)$.

Figure 5.4: Side view of different auto-generation cases (Case I) when eddies are aligned behind each other compared to the case of single eddy ($y_e^+ = 102.7$). The effect on auto-generation due to spacing between them is studied. All eddies are visualized by iso-surface of $\lambda_{ci}^2 = 30$. Left column is at $t^+ = 248.4$ and right column is at $t^+ = 349.2$.

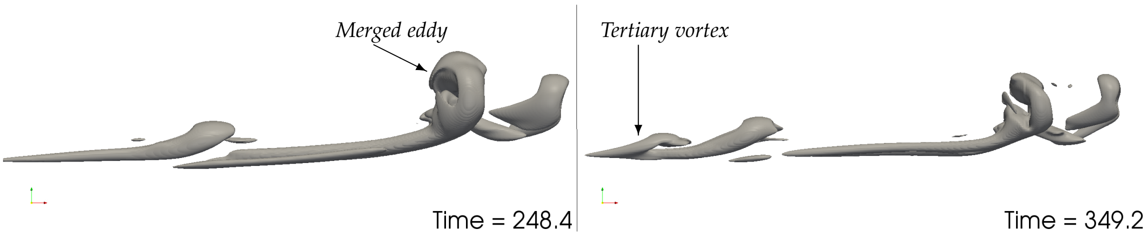

(a) Case II with $\Delta x^+ = 70.3$.

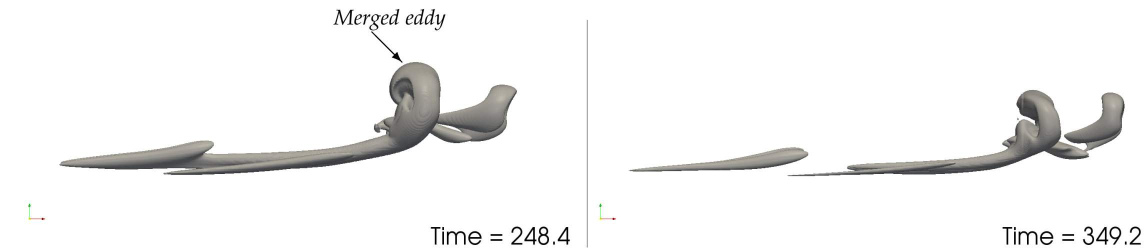

(b) Case II with $\Delta x^+ = 140.6$.

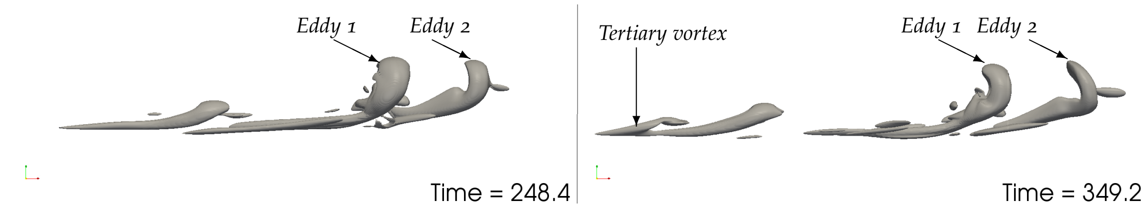

(c) Case III with $\Delta x^+ = 140.6$.

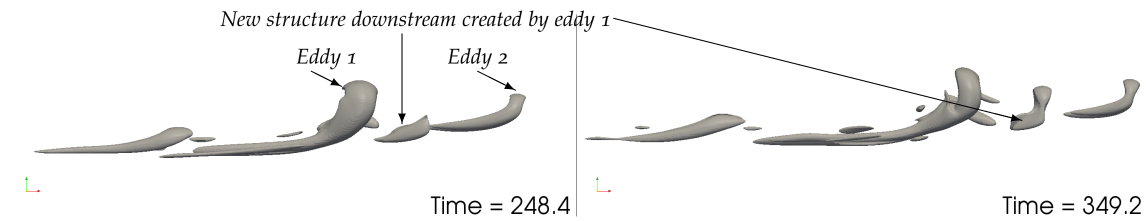

(d) Case III with $\Delta x^+ = 281.2$.

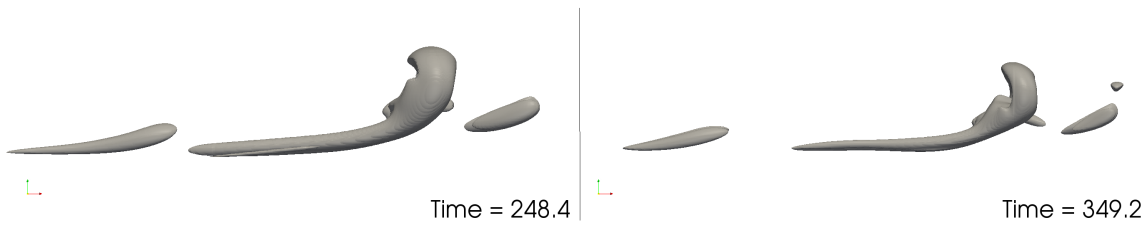

(e) Simulation of single eddy $(y_e^+, \alpha) = (68.9, 2)$.

Figure 5.5: Side view of different auto-generation cases (Case II & III) when eddies are aligned behind each other compared to the case of single eddy ($y_e^+ = 68.9$). All eddies are visualized by iso-surface of $\lambda_{ci}^2 = 30$. Left column is at $t^+ = 248.4$ and right column is at $t^+ = 349.2$.

The initial condition of case I contains two eddies which do not auto-generate individually. But when they are put together, new structures are generated which can be seen in figures 5.4a, 5.4b, 5.4c and 5.4d. In case II and III, one of the two eddies $(y_e^+, \alpha = 68.9, 2)$ auto-generates individually and is shown in figure 5.5e. Figures 5.5a, 5.5b 5.5c and 5.5d show the cases with two eddies where one eddy auto-generates individually. In these cases, formation of the tertiary vortex upstream can be observed in figures 5.5a and 5.5c. So compared to single eddy case (figure 5.5e), there is an enhancement in terms of generation of new structures. From this it can be inferred that there is an interaction between two eddies when aligned behind each other which leads to the generation of new structures. And also, the auto-generation can take place when two eddies which individually does not possess sufficient strength to auto-generate are aligned behind each other.

Figures 5.4a, 5.4b, 5.4c, 5.4d and 5.4e show the effect of spacing on generation of new structures. As the stream-wise distance (Δx^+) is increased from 70.3 to 421.9, the newly generated stream-wise vortices upstream are weaker. So with increasing Δx^+, the interaction which causes auto-generation weakens. This also suggests that the two eddies become independent of each other as spacing between the two grows. Merging takes place for the stream-wise spacing $\Delta x^+ = 70.3,\ 101$ and 140.6 (70.3 is an initial merged case) and also auto-generation occurs. Hence merging results in formation of stronger eddies of threshold strength. It can also be noted that the auto-generation occurs after merging, so there is no vortex-vortex interaction in these cases. Also there is no remarkable change in generation of new structures due to merging. So merging do not influence the trend of decreasing size of new structures with increasing stream-wise spacing. The vortex-vortex interaction decreases with increasing stream-wise spacing but still there is an interaction which can be seen in case of larger separation distance. This may be because both the eddies share the same low speed streak, due to which fluid ejected by downstream eddy is absorbed by upstream eddy. This is vortex-streak interaction.

For case III, where there is no merging for $\Delta x^+ = 140$, tertiary hairpin formation occurs (see figure 5.5c at $t^+ = 349.2$). The second eddy $y_e^+ = 102.7$ (eddy 2) remains as a downstream vortex and becomes stronger which can be seen by its increased size in figure 5.5c. For $\Delta x^+ = 281$, a new downstream eddy (located in between the two initial eddies) is created by the initial upstream eddy $y_e^+ = 68.9$ (eddy 1) as shown in figure 5.5d at $t^+ = 248.4$. This newly generated structure interacts with the second initial eddy downstream $y_e^+ = 102.7$ and becomes a hairpin as shown in figure 5.5d at $t^+ = 349.2$ which otherwise was just a pair of counter-rotating stream-wise vortex (see figure 5.5e).

From all these observations, it may be inferred that, vortex-vortex and vortex-streak interactions happen when the stream-wise spacing smaller. And vortex-streak interaction occurs when the separation distance is larger. Also merging or no merging, the interactions which lead to auto-generation will happen.

5.5 INTERPRETATION OF 2-DIMENSIONAL DATA

In this section, 2-d plots are analyzed and understood based on interpretation given in section 5.1.1 for the single eddy case. Figure 5.6 represents the 2-d data for the case I $(y_{e1}^+, y_{e2}^+) = (102.7, 68.9)$ with different stream-wise spacing (Δx^+). It also contains data of a single eddy case corresponding to $(y_e^+, \alpha) = (102.7, 2)$ for comparison.

In figure 5.6a, it can be observed that the growth rate (variation of the normalized maximum square of swirling strength (λ_{ci}^2) with respect time) and the amount of increase in the normalized maximum λ_{ci}^2, decrease as stream-wise spacing Δx^+ increases. The initial growth rate before the dot '•' is connected with the evolution of the pair of counter-rotating stream-wise vortices into primary hairpin similar to the observation in figure 5.1a. The maximum λ_{ci}^2 has a peak value of 5.09 for stream-wise spacing $\Delta x^+ = 70$ which is twice the value 2.7 in single eddy case. For $\Delta x^+ = 101,\ 140.6,\ 281.2$ and 481.9 the peak value of maximum λ_{ci}^2 is 3.61, 2.93, 2.83 and 2.78 respectively. As inferred in section 5.1.1, the higher the initial growth rate the faster is the development of initial eddy into a primary hairpin. So it can be implied that the primary hairpin formation takes longer as the spacing between eddies is increased, as growth rate decreases with increasing spacing. This is consistent with the 3-d observations.

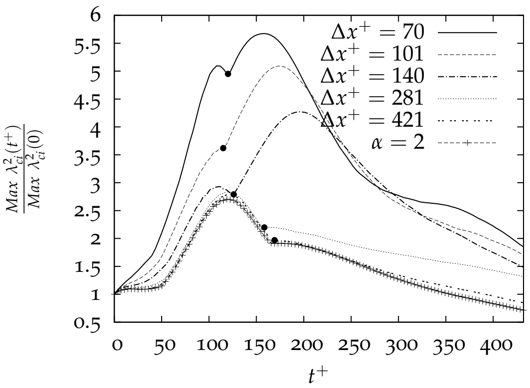

(a) Temporal evolution of the normalized maximum of λ_{ci}^2. Location of maximum λ_{ci}^2 shifting to stream-wise vortex legs from head is shown by dot •. $\alpha = 2$ represents single eddy case.

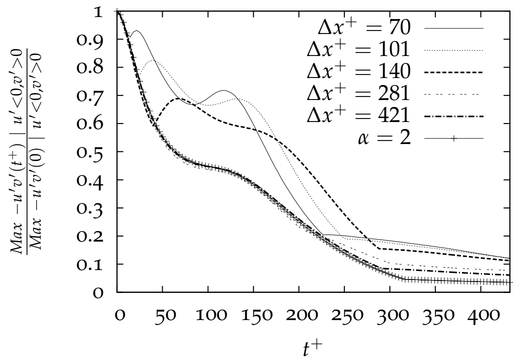

(b) Temporal evolution of the normalized maximum of $-u'v' \mid u' < 0, v' > 0$. $\alpha = 2$ represents single eddy case.

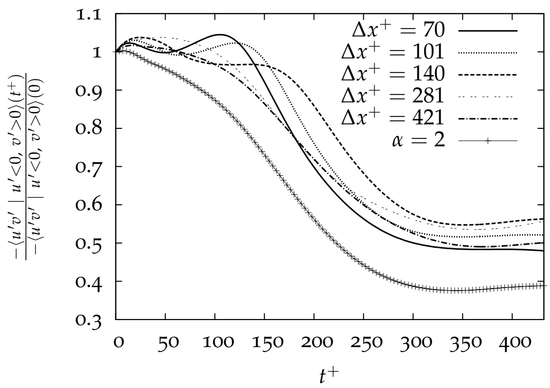

(c) Temporal evolution of the normalized volume average $-u'v' \mid u' < 0, v' > 0$. $\alpha = 2$ represents single eddy case.

Figure 5.6: Effect of initial stream-wise spacing (Δx^+) between eddies in Case I.

After the point '•', the location of normalized maximum square of swirling strength (λ_{ci}^2), shifts to the legs of stream-wise vortex. The maximum λ_{ci}^2 in the legs for the case of $\Delta x^+ = 70.3$, 101 and 140.6, increases and reaches peak values of 5.67, 5.09 and 4.27 respectively. The increase in max λ_{ci}^2 is much higher in case of the legs than in the head. For other stream-wise spacings, after point '•' maximum λ_{ci}^2 continues to decrease. From the interpretation made in section 5.1.1, new structures arise from higher swirling strength (λ_{ci}^2) in the legs which may lead to an instability in the legs resulting in creation of new structures. Hence it is expected that the new structures are produced for the case of $\Delta x^+ = 70.3$, 101 and 140.6. This is true and can be seen in figures 5.4a, 5.4b 5.4c.

From figure 5.6c, the amount of volume averaged Reynolds shear stress generated by ejections decreases with increasing stream-wise spacing (Δx^+). The cases of $\Delta x^+ = 70.3$, 101 and 140.6, show $-\langle u'v' \rangle$ increasing between $t^+ = 50 - 105$, $t^+ = 65 - 125$ and $t^+ = 110 - 140$ respectively compared to continuously decreasing trend for the other cases. Similar trend is seen for $-\langle u'v' \rangle$ in figure 5.1e for auto-generation of single eddy case $(\alpha = 3)$ compared to non-auto-generating cases $(\alpha = 1, 2)$. So from the figure 5.6c, it can be deduced that the case of $\Delta x^+ = 70.3$, 101 and 140.6 auto-generate.

The peaks of normalized maximum λ_{ci}^2, normalized $-\langle u'v' \rangle$ and normalized maximum $-u'v'$ happen approximately at the same time as shown table 5.2 for single eddy case in section 5.1.1. This trend is not observed in figures 5.6a, 5.6c and 5.6b.

6

CONCLUSIONS AND RECOMMENDATIONS

6.1 SUMMARY AND CONCLUSIONS

In this report, how a hairpin of certain threshold strength to auto-generate come into existence is investigated. To this end, the possibilities of vortex merger or interactions between two weak conditional eddies resulting in generation of stronger vortex has been studied by means of Direct Numerical Simulation (DNS). The weak conditional eddies cannot auto-generate individually. The initial conditional eddies were obtained from the linear stochastic estimation (LSE) procedure applied to a DNS database of fully developed turbulent plane channel flow at $Re_\tau = 360$. The DNS code was validated by comparing the turbulent flow statistics to the results of Kim et al. (1987) and the LSE procedure to the results of Zhou et al. (1999). Before studying the interaction between two conditional eddies, the single eddy case was studied to establish the base-line for comparison. The interactions and vortex merging between two non auto-generating eddies is investigated in different scenarios. These scenarios are created based on different initial strengths, initial sizes and initial spacing between the eddies. In all the cases, the two eddies were perfectly aligned behind each other in the stream-wise direction.

Merging of two eddies only occurred in the cases of the larger (higher y_e^+) eddy upstream followed by smaller (lower y_e^+) eddy downstream. This happens because the larger eddy upstream travels faster then the smaller eddy downstream. The larger eddy travels faster due to higher mean flow velocity at larger distance from wall. There was no merging in the reverse case where smaller eddy upstream was followed by a larger eddy downstream. After merging, the geometric shape of the new structure broadly remained similar to the hairpin structure. The merging is consistent with experimental observations described in Elsinga et al. (2012).

For the case of a large eddy upstream followed by a small eddy downstream, merging was found to be a function of the initial spacing and the initial strength of eddies. If the eddies are within a certain initial stream-wise distance like $\Delta x^+ = 140$ for case I, merging occurred but above that there was no merging. As the stream-wise spacing (Δx^+) increased, the interaction between the eddies reduced. For the same spacing $\Delta x^+ = 140$ and different strength of two eddies (see figures 5.3b and 5.3d), it was observed that the merging happens quicker and is clearer when the smaller downstream eddy has higher strength. The two eddies are pulled closer to each other much faster in case of the stronger, smaller eddy downstream. The amount of fluid pumped upstream between the legs of the downstream eddy increases with its strength. Hence the faster approach of the two eddies may be due to the absorption of the fluid by the upstream eddy from the downstream eddy.

In the current study, auto-generation is loosely referred to creation of new structures whether hairpins or pairs of quasi-stream-wise vortices. The presence of interaction between two eddies was identified by looking at auto-generation. New structures are created, when two eddies, which individually do not auto-generate are aligned behind each other. This is seen in figures 5.4a, 5.4b, 5.4c, 5.4d and 5.4e. Even in the case of two eddies with one auto-generating individually and the other one not, there is an enhancement in the creation of new structures like tertiary hairpins (see figures 5.5a and 5.5c). From this it can be concluded that when two eddies are aligned behind each other, there is an interactions between two eddies which leads to auto-generation.

In case I, it is observed that the size of the new structures decreases for increasing initial stream-wise spacing (see figures 5.4a, 5.4b, 5.4c, 5.4d and 5.4e). The new structures develop much faster in time when the separation distance between the eddies decreases as can be observed in the movies attached. Merging takes place for cases with stream-wise spacing $\Delta x^+ = 70.3$, 101 and 140.6 before auto-generation occurs. So the auto-generation is not caused by vortex-vortex interaction as the eddies have already been merged. But it is caused by the merging of two weak eddies into a single stronger eddy. From the figures, it can also be noted that there is no remarkable in generation of new structures due to merging. So merging do not influence the trend of decreasing size of new structures with increasing stream-wise spacing. The vortex-vortex interaction weakens with increasing stream-wise spacing but still there is an interaction in case of higher spacing. This may be because both the eddies share the same low speed streak, due to which fluid ejected by downstream eddy is absorbed by upstream eddy. This leads to vortex-streak interactions. The non-merging cases like case III and case IV, with smaller upstream and larger eddy downstream, show enhancement in auto-generation. In case III, where one is auto-generating individually and other do not, tertiary hairpin formation can be seen in figure 5.5c.

From all these observations, it may be concluded that, vortex-vortex and vortex-streak interactions happen when the stream-wise spacing smaller. And vortex-streak interaction occurs when the separation distance is larger. Also merging or no merging, the interactions which lead to auto-generation will happen.

It is also concluded that, when two non-auto-generating eddies are separated by a sufficiently small stream-wise spacing then merging takes place. This results in the formation of a stronger eddy which can auto-generate. Hence merger is a viable explanation for the creation of threshold strength eddies. It extends the auto-generation process towards a possible self-sustaining mechanism meaning: two initial hairpins merge producing a strong hairpin, which creates a new hairpin structure by auto-generation resulting again in two hairpins.

From vortex-streak interaction, it may be concluded that low-speed streak does play a role in the generation of new structures. Hence the criterion and the mechanisms to determine the auto-generation become more complex when two hairpins are aligned behind each other than the one mentioned (threshold strength) for a single eddy case in Zhou et al. (1999).

6.2 RECOMMENDATIONS

- All the simulations in this study were conducted at a low Reynolds number Re_τ=360. High Reynolds number simulations are recommended to show that this theory is robust and unambiguous.

- What kinds of merging occur in real turbulent flows needs to be investigated experimentally and numerically. Possible other merging cases (those not covered by the present study) need to be studied in an ideal numerical setup like the present study to extend this theory further.

- In the present simulations, the two eddies are on the same low speed streak. So it is important to study if this low speed streaks play a role in merging and auto-generation and how.
- In Zhou et al. (1999) it was noted that the distance between the primary and the secondary hairpin is higher in the symmetric case than the non-symmetric hairpin case. The spacing in the non-symmetric hairpin case is found to be closer to the spacing found in experiments. Hence simulations of initial condition involving non-symmetric eddies should be done to study the effect of spacing between vortices on merging and auto-generation.

A

NUMERICAL METHODS

A.1 TIME INTEGRATION: RUNGE-KUTTA SCHEME

$$C(u_i) = \frac{\partial u_j u_i}{\partial x_j}$$

$$D(u_i) = \frac{1}{Re_\tau}\frac{\partial^2 u_i}{\partial x_i^2}$$

$\dfrac{\partial p_b}{\partial x_i}$ a constant pressure gradient

$n - \dfrac{1}{2}$ is given by m

$n + \dfrac{1}{2}$ is given by m+1

Runge-Kutta: Step 1

$$\begin{aligned}
u_i^* &= u_i^n + dt \cdot \frac{32}{60}\left(-\frac{\partial p_b}{\partial x_i} - \frac{\partial p^m}{\partial x_i} - C(u_i^n) + D(u_i^n)\right)\\
\frac{\partial^2(\delta p)}{\partial x_i^2} &= \frac{1}{dt(\frac{32}{60})} \cdot \frac{\partial u_i^*}{\partial x_i}\\
p^{m*} &= p^m + \delta p\\
u_i^{n*} &= u_i^* - dt \cdot \frac{32}{60} \cdot \frac{\partial(\delta p)}{\partial x_i}
\end{aligned}$$

Runge-Kutta: Step 2

$$\begin{aligned}
u_i^{**} &= u_i^{n*} + dt \cdot \frac{8}{60}\left(-\frac{\partial p_b}{\partial x_i} - \frac{\partial p^{m*}}{\partial x_i}\right) + dt \cdot \frac{25}{60}\left(-C(u_i^{n*}) + D(u_i^{n*})\right)\\
&\quad - dt \cdot \frac{17}{60}\left(-C(u_i^n) + D(u_i^n)\right)\\
\frac{\partial^2(\delta p)}{\partial x_i^2} &= \frac{1}{dt(\frac{8}{60})} \cdot \frac{\partial u_i^{**}}{\partial x_i}\\
p^{m**} &= p^{m*} + \delta p\\
u_i^{n**} &= u_i^{**} - dt \cdot \frac{8}{60} \cdot \frac{\partial(\delta p)}{\partial x_i}
\end{aligned}$$

Runge-Kutta: Step 3

$$
\begin{aligned}
u_i^{***} &= u_i^{n**} + dt \cdot \frac{20}{60}\left(-\frac{\partial p_b}{\partial x_i} - \frac{\partial p^{m**}}{\partial x_i}\right) + dt \cdot \frac{45}{60}\left(-C(u_i^{n**}) + D(u_i^{n**})\right) \\
&\quad - dt \cdot \frac{25}{60}(-C(u_i^{n*}) + D(u_i^{n*})) \\
\frac{\partial^2(\delta p)}{\partial x_i^2} &= \frac{1}{dt(\frac{20}{60})} \cdot \frac{\partial u_i^{***}}{\partial x_i} \\
p^{m+1} &= p^{m**} + \delta p \\
u_i^{n+1} &= u_i^{***} - dt \cdot \frac{20}{60} \cdot \frac{\partial(\delta p)}{\partial x_i}
\end{aligned}
$$

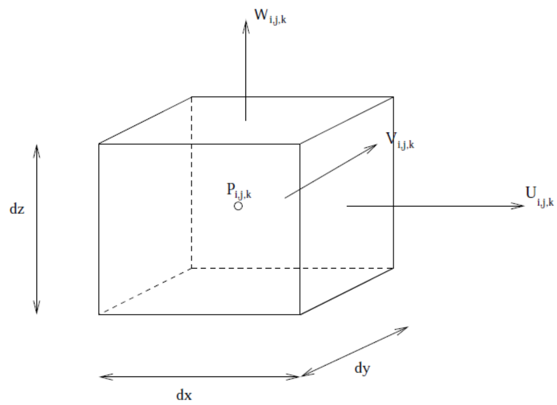

Figure A.1: Staggered Grid.

A.2 SPATIAL DISCRETISATION: CONTINUITY AND MOMENTUM EQUATIONS

Continuity equation is discretized at pressure points as shown in figure A.1 and is given by

$$
\begin{aligned}
\frac{\partial u_i}{\partial x_i} = \frac{1}{dx}\big(u(i,j,k) - u(i-1,j,k)\big) + \frac{1}{dy}\big(v(i,j,k) - v(i,j-1,k)\big) \\
+ \frac{1}{dz}\big(w(i,j,k) - w(i,j,k-1)\big) \qquad \text{(A.1)}
\end{aligned}
$$

X-momentum equation is discretized with u velocity point as center of the cell. Similarly y and z momentum is calculated with respective velocity point as center of cell.

Convective terms $C(u_i)$ for x-momentum are given by

$$
\frac{\partial uu}{\partial x} = \frac{1}{dx}\left(\left[\frac{u(i+1,j,k) + u(i,j,k)}{2}\right]^2 - \left[\frac{u(i,j,k) + u(i-1,j,k)}{2}\right]^2\right) \qquad \text{(A.2)}
$$

$$
\begin{aligned}
\frac{\partial uv}{\partial y} &= \frac{1}{dy}\left(\left[\left(\frac{u(i,j,k) + u(i,j+1,k)}{2}\right)\left(\frac{v(i+1,j,k) + v(i,j,k)}{2}\right)\right]\right. \\
&\quad \left. - \left[\left(\frac{u(i,j,k) + u(i,j-1,k)}{2}\right)\left(\frac{v(i+1,j-1,k) + v(i,j-1,k)}{2}\right)\right]\right) \qquad \text{(A.3)} \\
\frac{\partial uw}{\partial z} &= \frac{1}{dz}\left(\left[\left(\frac{u(i,j,k+1) + u(i,j,k)}{2}\right)\left(\frac{w(i+1,j,k) + w(i,j,k)}{2}\right)\right]\right.
\end{aligned}
$$

$$- \left[\left(\frac{u(i,j,k)+u(i,j,k-1)}{2}\right)\left(\frac{w(i+1,j,k-1)+w(i,j,k-1)}{2}\right)\right]\Bigg) \quad \text{(A.4)}$$

Viscous terms $D(u_i)$ are given by

$$\frac{1}{Re_\tau}\frac{\partial^2 u}{\partial x^2} = \frac{1}{Re_\tau \cdot dx}\left(\frac{u(i+1,j,k)-u(i,j,k)}{dx} - \frac{u(i,j,k)-u(i-1,j,k)}{dx}\right) \quad \text{(A.5)}$$

$$\frac{1}{Re_\tau}\frac{\partial^2 u}{\partial y^2} = \frac{1}{Re_\tau \cdot dy}\left(\frac{u(i,j+1,k)-u(i,j,k)}{dy} - \frac{u(i,j,k)-u(i,j-1,k)}{dy}\right) \quad \text{(A.6)}$$

$$\frac{1}{Re_\tau}\frac{\partial^2 u}{\partial z^2} = \frac{1}{Re_\tau \cdot dz}\left(\frac{u(i,j,k+1)-u(i,j,k)}{dz} + \frac{u(i,j,k)-u(i,j,k-1)}{dz}\right) \quad \text{(A.7)}$$

A.3 VELOCITY GRADIENT TENSOR

Velocity gradient at the center of the cell(pressure point) is given by

$$\frac{\partial u}{\partial x} = \frac{u(i,j,k)-u(i-1,j,k)}{dx}$$

$$\frac{\partial v}{\partial y} = \frac{v(i,j,k)-v(i,j-1,k)}{dy}$$

$$\frac{\partial w}{\partial z} = \frac{w(i,j,k)-w(i,j,k-1)}{dz}$$

$$\frac{\partial u}{\partial y} = \frac{1}{dy}\left[\left(\frac{u(i-1,j,k)+u(i-1,j+1,k)+u(i,j+1,k)+u(i,j,k)}{4}\right) - \left(\frac{u(i-1,j,k)+u(i-1,j-1,k)+u(i,j-1,k)+u(i,j,k)}{4}\right)\right]$$

$$\frac{\partial u}{\partial z} = \frac{1}{dz}\left[\left(\frac{u(i-1,j,k)+u(i-1,j,k+1)+u(i,j,k+1)+u(i,j,k)}{4}\right) - \left(\frac{u(i-1,j,k)+u(i-1,j,k-1)+u(i,j,k-1)+u(i,j,k)}{4}\right)\right]$$

$$\frac{\partial v}{\partial x} = \frac{1}{dx}\left[\left(\frac{v(i+1,j,k)+v(i+1,j-1,k)+v(i,j,k)+v(i,j-1,k)}{4}\right) - \left(\frac{v(i-1,j,k)+v(i-1,j-1,k)+v(i,j,k)+v(i,j-1,k)}{4}\right)\right]$$

$$\frac{\partial v}{\partial z} = \frac{1}{dz}\left[\left(\frac{v(i,j,k+1)+v(i,j-1,k+1)+v(i,j,k)+v(i,j-1,k)}{4}\right) - \left(\frac{v(i,j,k-1)+v(i,j-1,k-1)+v(i,j,k)+v(i,j-1,k)}{4}\right)\right]$$

$$\frac{\partial w}{\partial x} = \frac{1}{dx}\left[\left(\frac{w(i+1,j,k)+w(i+1,j,k-1)+w(i,j,k)+w(i,j,k-1}{4}\right) - \left(\frac{w(i-1,j,k)+w(i-1,j,k-1)+w(i,j,k)+w(i,j,k-1}{4}\right)\right]$$

$$\frac{\partial w}{\partial y} = \frac{1}{dy}\left[\left(\frac{w(i,j+1,k)+w(i,j+1,k-1)+w(i,j,k)+w(i,j,k-1}{4}\right) - \left(\frac{w(i,j-1,k)+w(i,j-1,k-1)+w(i,j,k)+w(i,j,k-1}{4}\right)\right]$$

B

DEVELOPMENT OF THE CONDITIONAL EDDY

B.1 PRIMARY HAIRPIN VORTEX

Conditional eddy in the initial condition will rapidly develop into a hairpin vortex which will be referred as primary hairpin. Evolution of primary hairpin is same for all the initial conditions mentioned in table 5.1. Development of conditional eddy can be seen in figure B.1. From figures, it can be observed that the initial eddy ($t_e^+ = 0$) lifts up with time. This lift up is due to mutual induction of velocity by one leg over another. Downstream end lifts faster because the span-wise distance between the legs is smaller than the upstream end. Lifting at the upstream end(legs) near the wall is retarded by vortex stretching which makes the legs thinner thereby reducing the mutual induction. In figures, at $t^+ = 72$, it can be noticed that the downstream end lifts up almost vertically and a span-wise vortex connects both quasi-stream-wise vortices. This process of curling up leading to formation of head is explained as follows.

The quasi-stream-wise vortices pump fluid up between their legs away from the boundary. This pumped up fluid encounters mean flow and forms a shear layer above the quasi-stream-wise vortices between the legs. As the swirling strength is higher in the downstream end of quasi-stream-wise vortices the associated shear layer is intense in that region. This intense shear layer rolls up into a span-wise vortex which can be seen in attached vorticity movie. As the legs are lifted in downstream end due to mutual induction, shear layer intensifies due to higher mean flow increasing the strength of span-wise vortex. Due to viscosity, this span-wise vortex connects the quasi-stream-wise vortices and forms head of the hairpin.The development of the initial structure to hairpin vortex observed in this study is consistent with the one mentioned in Zhou et al. (1999).

B.2 SELF INDUCED MOTIONS IN HAIRPINS AND THEIR DEVELOPMENT

Formation and evolution of Ω-shaped hairpin, as shown in figure B.1 ($t^+ = 144$), can be explained by self and mutual induction mechanisms as shown in figure B.2 from Zhou et al. (1999). Before explaining the mechanisms associated with development of primary hairpin, self-induction is described briefly. Velocity($\mathbf{u}$) of a line vortex with no viscosity at any point $\mathbf{x}'$ is given by

$$\mathbf{u}(\mathbf{x}) = -\frac{\kappa}{4\pi} \oint \frac{(\mathbf{x}-\mathbf{x}') \times d\mathbf{l}(\mathbf{x}')}{|\mathbf{x}-\mathbf{x}'|^3} \tag{B.1}$$

where $\mathbf{x}'$ represents point on vortex, $d\mathbf{l}(\mathbf{x}')$ is line element along the vortex, κ is vortex strength. Now hairpin vortex is assumed to be thin, isolated vortex tube. Now effect of curvature of the vortex on velocity on an adjacent point needs to be investigated. If velocity has a component apart from circulatory motion component, it contributes to the

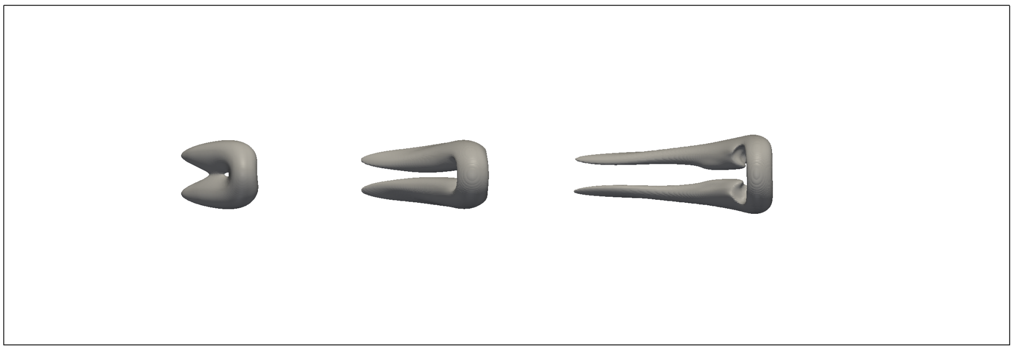

(a) Top view of the development of conditional eddy.

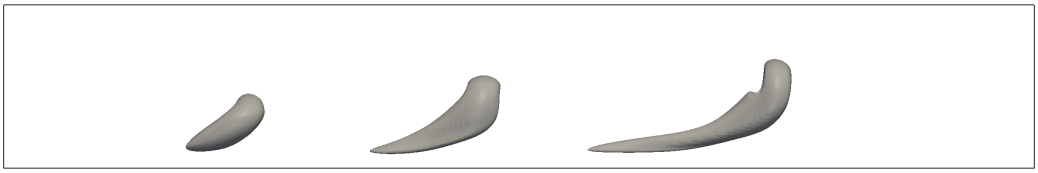

(b) Front view of the development of the conditional eddy.

Figure B.1: Formation of primary hairpin vortex for initial condition $(y_e^+, \alpha) = (102.7, 2)$.

shifting of line vortex which is caused due to self induction. From Bachelor (1967), self induced velocity component due to curvature is given by

$$\frac{\kappa c}{4\pi}\mathbf{b}log\frac{L}{\sigma} \tag{B.2}$$

where σ is thickness of vortex tube, L is length of line vortex, c and $\mathbf{b}$ are local curvature and bi-normal vector at a point in the vortex curve.

FIGURE B.2 (a) The hairpin head lifts up almost vertically which leads to strong local curvature at points as indicated by B, B' in figure. From equation B.2, due to the strong curvature self induced motion pushes the legs apart from each other in the span-wise direction and the head is pushed up in the direction of downstream flow as shown in figure.

FIGURE B.2 (b) Vortex-wall interaction tries to bring the legs closer which mitigates the self induced motion in span-wise direction. This can be explained by image vortex concept. This effect decreases with increasing distance from the wall. Hence the span-wise distance between two legs increases with distance from the wall leading to the formation of Ω shaped hairpin. Self induction by this new curvature near the neck as indicated by C, C' pushes the legs at that point towards the wall as shown in the figure.

FIGURE B.2 (c) As the region near neck moves towards the wall due to self induction and the whole hairpin lifts up due to mutual induction. This causes a slight negative tilt near the neck region. This creates a new curvature as indicated in figure by D, D'. Self

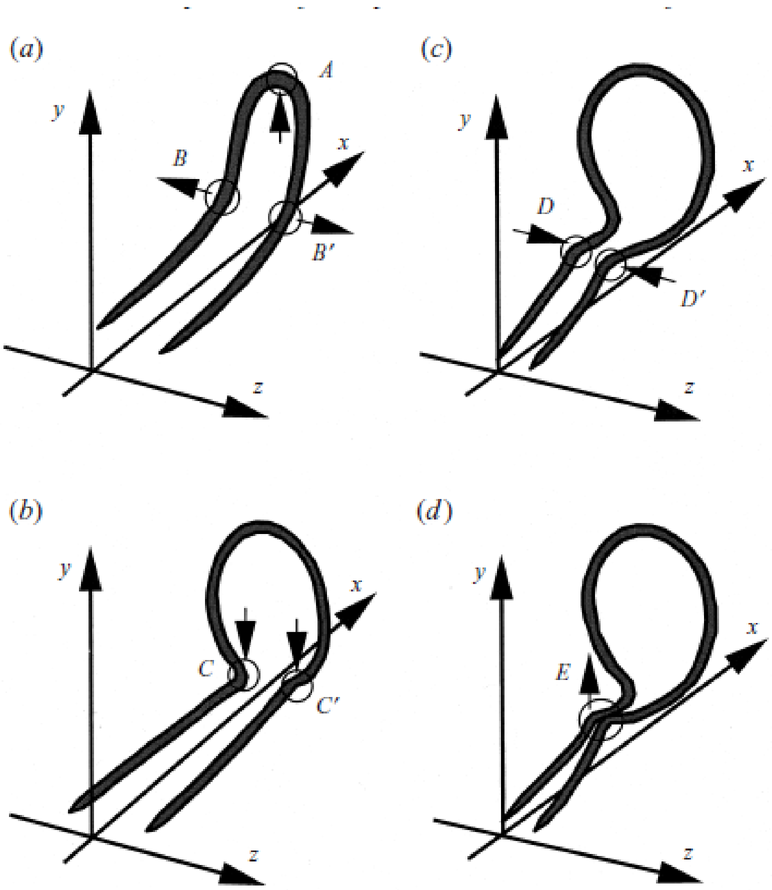

Figure B.2: Self induced motion of a hairpin vortex. (taken from Zhou et al., 1999).

induced effect due to this curvature results in bringing the legs towards each other near that curvature as shown in figure.

FIGURE B.2 (d) As points marked D, D' move closer to each other in figure B.2c, the mutual induction increases and thereby lifts up that portion. This lift up results in formation of a kink as marked E in figure B.2(d).

This kink continues to rise and breaks away from primary hairpin leading to formation of secondary hairpin vortex (SHV). SHV undergoes above mentioned process leading to formation of new hairpins as shown in figures B.3a and B.3b.

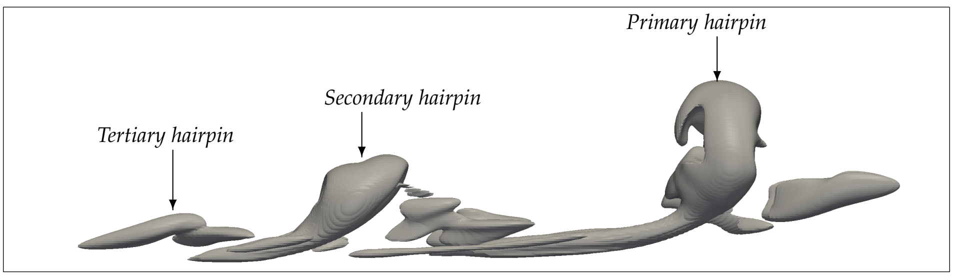

(a) Side view.

Figure B.3: Formation of secondary and tertiary hairpin vortices. *(cont.)*

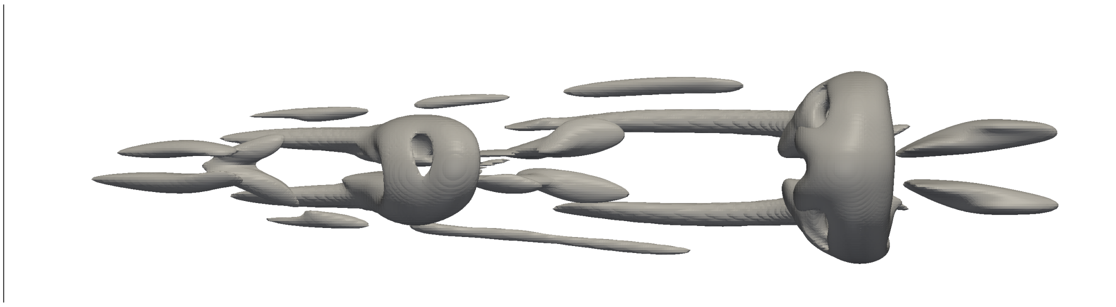

(b) Top view.

Figure B.3: Formation of secondary and tertiary hairpin vortices.

B.3 BASE LINE STUDIES

B.3.1 *Different swirling strength at same event location*

Figure B.4, B.5 shows two eddies (one black and other gray) which are simulated individually as single eddy cases. They are overlapped in visualization to study the difference in evolution. Conditional eddy with higher local swirling strength (λ_{ci}) travels at the same speed or slightly slower speed then the lower λ_{ci} for event specified at same point.

(a) Side view.

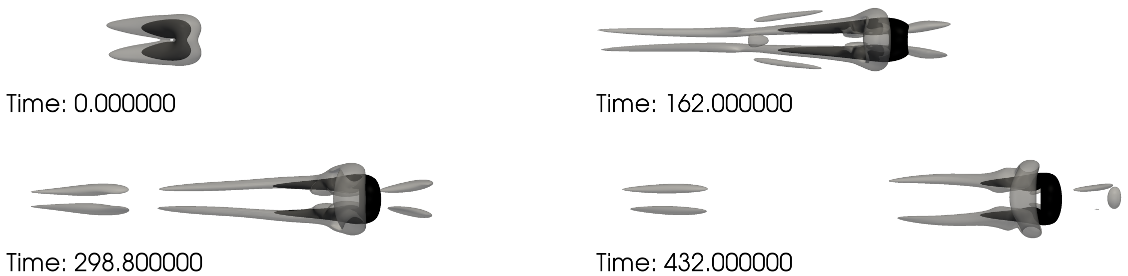

(b) Top view.

Figure B.4: Two overlapped hairpins at $y_e^+ = 68.9$ with $\alpha = 1$(black) and $\alpha = 2$(gray). Time is in t^+ units.

B.3.2 *Different event location and same swirling strength*

Figure B.6 shows two eddies (one black and other gray) which are simulated individually as single eddy cases. They are overlapped in visualization to study the difference in

(a) Side view.

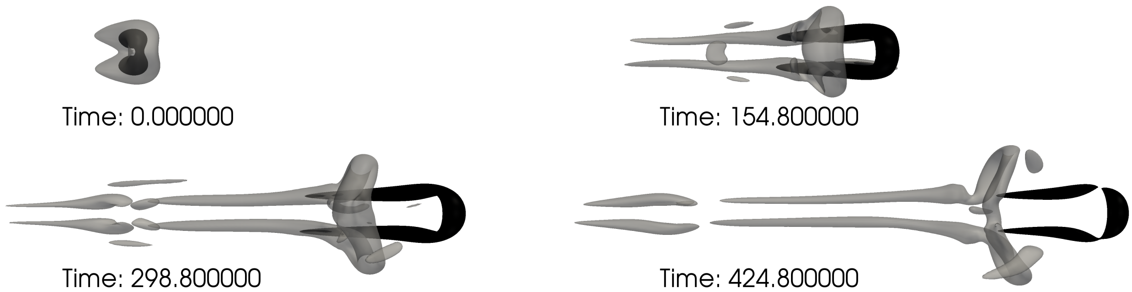

(b) Top view.

Figure B.5: Two overlapped hairpins at $y_e^+ = 102.7$ with $\alpha = 1$(black) and $\alpha = 3$(gray). Time is in t^+ units.

evolution. From figure B.6, it can be concluded that the conditional eddy based on event specified at higher y^+ travels faster for same swirling strength.

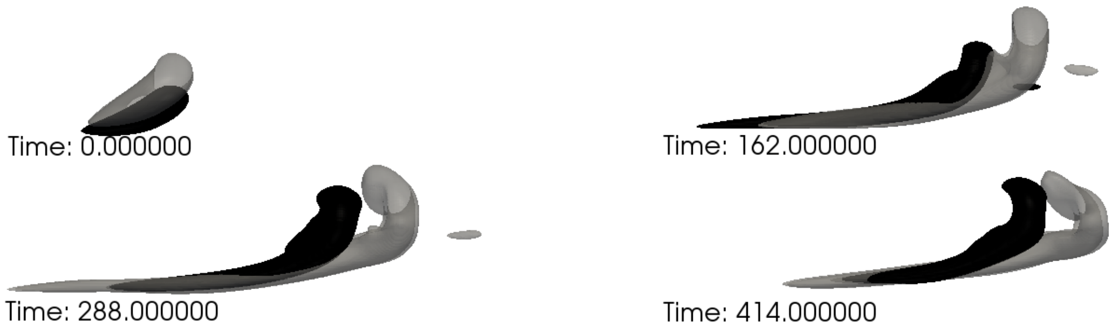

(a) Side view.

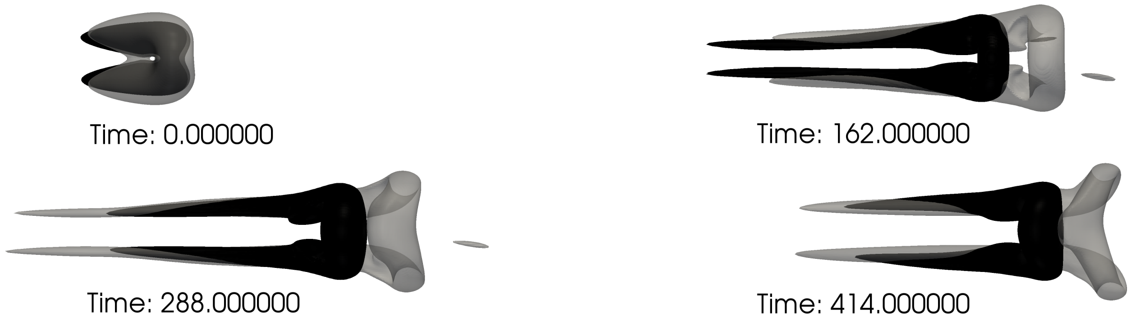

(b) Top view.

Figure B.6: Two overlapped hairpins at $y_e^+ = 68.9$(black) and $y_e^+ = 102.7$(gray) with approximately same swirling strength. Time is in t^+ units.

B.3.3 *2-d plots for* $y_e^+ = 68.9$

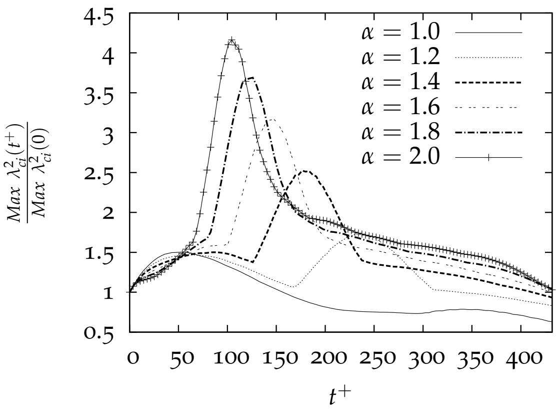

(a) Normalized maximum of λ_{ci}^2.

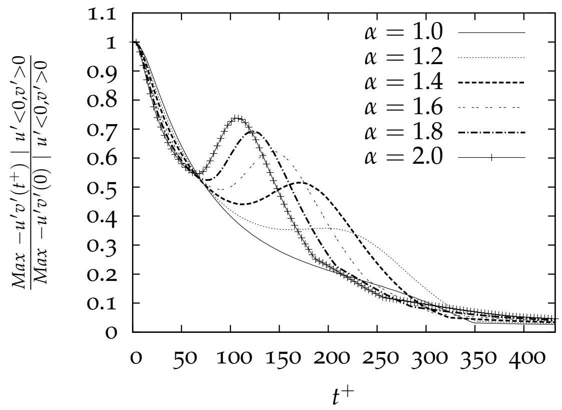

(b) Normalized maximum of $-u'v' \mid u' < 0, v' > 0$.

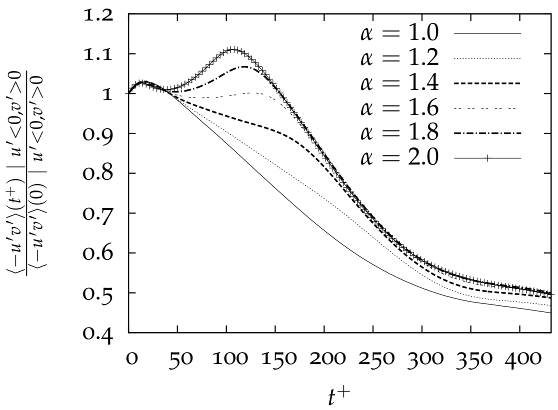

(c) Normalized volume average $-u'v' \mid u' < 0, v' > 0$.

Figure B.7: Temporal evolution of (a) Normalized maximum of the square of swirling strength (λ_{ci}^2). (b) Normalized maximum of Reynolds shear stress $-u'v'$ where $u' < 0, v' > 0$ (ejection event). (c) Normalized volume average of Reynolds shear stress ($-\langle u'v' \rangle$ where $u' < 0, v' > 0$). for single initial eddy at $y_e^+ = 68.9$. All values are normalized with their initial value at $t^+ = 0$.

BIBLIOGRAPHY

R. J. Adrian. Stochastic estimation of conditional structure: a review. *Applied Scientific Research*, 53:291–303, December 1994. ISSN 0003-6994, 1573-1987. doi: 10.1007/BF00849106. URL http://www.springerlink.com/content/p7032j15r77pp7p7/.

R. J. Adrian. Stochastic estimation of the structure of turbulent fields. In J. P Bonnet, editor, *Eddy structure identification*, number 353 in CISM International Centre for Mechanical Sciences, pages 145–196. Springer-Verlag, 1996.

R. J. Adrian. Hairpin vortex organization in wall turbulence. *Physics of Fluids*, 19:041301, 2007. ISSN 10706631. doi: 10.1063/1.2717527. URL http://pof.aip.org/resource/1/phfle6/v19/i4/p041301_s1.

R. J. Adrian, C. D. Meinhart, and C. D. Tomkins. Vortex organization in the outer region of the turbulent boundary layer. *Journal of Fluid Mechanics*, 422:1–54, 2000. doi: null. URL http://dx.doi.org/10.1017/S0022112000001580.

G. K Bachelor. *An Introduction to Fluid Dynamics*, chapter 7, pages 509–511. Cambridge University Press, London, 1967.

P. Bandyopadhyay. Large structure with a characteristic upstream interface in turbulent boundary layers. *Physics of Fluids*, 23:2326, 1980. ISSN 00319171. doi: 10.1063/1.862928. URL http://pof.aip.org/resource/1/pfldas/v23/i11/p2326_s1.

G. E. Elsinga, R. J. Adrian, B. W. Van Oudheusden, and F. Scarano. Three-Dimensional vortex organization in a High-Reynolds-Number supersonic turbulent boundary layer. *Journal of Fluid Mechanics*, 644:35–60, 2010. doi: 10.1017/S0022112009992047.

G. E. Elsinga, C. Poelma, A. Schröder, R. Geisler, F. Scarano, and J. Westerweel. Tracking of vortices in a turbulent boundary layer. *Journal of Fluid Mechanics*, 697:273–295, 2012. doi: 10.1017/jfm.2012.60. URL http://dx.doi.org/10.1017/S0022112012000602.

B. Ganapathisubramani, Ellen K. Longmire, and Ivan Marusic. Characteristics of vortex packets in turbulent boundary layers. *Journal of Fluid Mechanics*, 478:35–46, 2003. doi: 10.1017/S0022112002003270. URL http://dx.doi.org/10.1017/S0022112002003270.

A. H. Haidari and C. R. Smith. The generation and regeneration of single hairpin vortices. *Journal of Fluid Mechanics*, 277:135–162, 1994. doi: 10.1017/S0022112094002715. URL http://dx.doi.org/10.1017/S0022112094002715.

M. R. Head and P. Bandyopadhyay. New aspects of turbulent boundary-layer structure. *Journal of Fluid Mechanics*, 107:297–338, 1981. doi: 10.1017/S0022112081001791. URL http://dx.doi.org/10.1017/S0022112081001791.

J. Kim, P. Moin, and R. Moser. Turbulence statistics in fully developed channel flow at low Reynolds number. *Journal of Fluid Mechanics*, 177:133–166, April 1987. doi: 10.1017/S0022112087000892. URL http://dx.doi.org/10.1017/S0022112087000892.

K. Kim, H. J. Sung, and R. J. Adrian. Effects of background noise on generating coherent packets of hairpin vortices. *Physics of Fluids*, 20:105107, 2008. ISSN 10706631. doi: 10.1063/1.3001797. URL http://pof.aip.org/resource/1/phfle6/v20/i10/p105107_s1.

A. E. Perry and Ivan Marusic. A wall-wake model for the turbulence structure of boundary layers. part 1. extension of the attached eddy hypothesis. *Journal of Fluid Mechanics*, 298:361–388, 1995. doi: 10.1017/S0022112095003351. URL http://dx.doi.org/10.1017/S0022112095003351.

S. K. Robinson. Coherent motions in the turbulent boundary layer. *Annual Review of Fluid Mechanics*, 23:601–639, January 1991. ISSN 0066-4189, 1545-4479. doi: 10.1146/annurev.fl.23.010191.003125. URL http://www.annualreviews.org/doi/abs/10.1146/annurev.fl.23.010191.003125.

C. R. Smith. A synthesized model of the near-wall behavior in turbulent boundary layers. In *Proceedings of the 8th Symposium of Turbulence*, Rolla, 1984. University of Missouri-Rolla.

C. R. Smith, J. D. A. Walker, A. H. Haidari, and U. Sobrun. On the dynamics of near-wall turbulence. *Philosophical Transactions: Physical Sciences and Engineering*, 336(1641): pp. 131–175, 1991. ISSN 09628428. URL http://www.jstor.org/stable/53882.

T. Theodorsen. Mechanism of turbulence. In *In Proc. Second Midwestern Conf. of Fluid Mechanics*, pages 1–19, Columbus, Ohio, 1952. Ohio State University.

J. Zhou, R. J. Adrian, S. Balachandar, and T. M. Kendall. Mechanisms for generating coherent packets of hairpin vortices in channel flow. *Journal of Fluid Mechanics*, 387: 353–396, 1999.